



Mineralogy and geochemistry of multi-coloured sapphires at the Portezuelo de Pajas Blancas' deposits, northern Chile: revealing crystal growth processes

Gustavo Miranda-Díaz^{1,2} · Andrew Menzies³ · Karl Riveros-Jensen² · Gerhard Heide¹ · Lena Bußmann⁴ · Birk Härtel⁵ · Roald Tagle³ · Eduardo Medina⁶ · Wolfgang Griem²

Received: 12 June 2023 / Accepted: 23 January 2024
© The Author(s) 2024

Abstract

Portezuelo de Pajas Blancas' primary metasomatic deposits host sapphires that differ in size, colour, and colour distribution through different lithological units. The discovery of sapphire-bearing secondary aeolian placer deposits enabled a detailed analysis of sapphire types to determine the causes of this heterogeneity. Representative single sapphires from the primary and secondary deposits were analysed using various techniques, including SEM-CL, OM-CL, Micro-XRF, Raman spectroscopy, and polarised transmitted light multi-focus optical microscopy. Based on the results, seven sapphire types were identified according to their colours and colour distribution. Fe and Ti concentrations mainly contribute to the colour and micro-textures occurrence. The primary growth textures include cores, progressive, oscillatory, and diffusion zoning, whereas the secondary alteration features correspond to micro-brecciation, re-arrangement, and overgrowth. Inclusions such as euhedral andalusite, anhedral anhydrite, and anhedral rutile were identified in the sapphires. The formation of Portezuelo de Pajas Blancas sapphires can be divided into five genetic stages: (i) core growth development; (ii) chemical imbalance due to open system behaviour that produces progressive and oscillatory zoning; (iii) low-temperature deformations that produce micro-brecciation; (iv) re-arrangement of pre-formed sapphire fragments and subsequent sapphire overgrowth; (v) diffusion zoning that produce Fe- and Ti-enriched outer rims. In conclusion, the Portezuelo de Pajas Blancas' sapphires were formed through at least five stages of oxidised contact metasomatism at varying temperatures and low pressures, where a heterogeneous forming condition predominates during sapphire formation.

Keywords Sapphire · Atacama · Metasomatic · Micro-textures · Geochemistry · Origin

✉ Gustavo Miranda-Díaz
gustavo.miranda@daad-alumni.de

- ¹ Institut Für Mineralogie, Technische Universität Bergakademie Freiberg, Brennhausgasse 14, 09599 Freiberg, Germany
- ² Departamento de Geología, Universidad de Atacama, Avenida Copayapu 485, 1531772 Copiapó, Chile
- ³ Bruker Nano GmbH, Am Studio 2D, 12489 Berlin, Germany
- ⁴ Institut Für Glas Und Glastechnologie, Zentrum Für Effiziente Hochtemperatur-Stoffwandlung (ZeHS), Technische Universität Bergakademie Freiberg, Winklerstraße 5, 09599 Freiberg, Germany
- ⁵ Department of Geoscience, University of Calgary, 2500 University Drive NW, Calgary, AB, Canada
- ⁶ Departamento de Ingeniería en Minas, Universidad de Antofagasta, Avenida Universidad de Antofagasta 02800, 1271155 Antofagasta, Chile

Introduction

The Portezuelo de Pajas Blancas (PPB) sapphire-rich metasomatites were discovered by the Exploraberg company in 2003. Berg and Tidy (2009) conducted the first geological study, whilst Miranda-Díaz et al. (2022) provided a detailed petrographic and mineralogical analysis. This primary metasomatic deposit shows an extension of around 1000 m² and contains granoblastic sapphires in almost all lithological units. The deposit also hosts variable abundances of tourmaline (mainly dravite), böhmite, diaspore, alunite, andalusite, and sillimanite. The sapphire-rich units display straight and well-defined contacts, whilst the boundaries between the deposit and the unmineralised rocks are not exposed. The proposed origin for this deposit is related to high-temperature contact metasomatism, where de-silicification processes linked to the intrusion of a Lower Cretaceous magmatic

body into Jurassic volcanic rocks through the Atacama fault system allowed the sapphires formation (Miranda-Díaz et al. 2022).

In this contribution, we present a complete reconstruction of metasomatic processes related to the sapphire's formation, specifying their forming conditions which allow an understanding of why the PPB sapphires show a broad range of colours, colour distributions, and sizes. This work also provides information on discovering the secondary aeolian placer deposit, spatially related to the primary metasomatite. For this, a detailed mineralogical and geochemical study was carried out in a representative population of sapphires from primary and secondary deposits, revealing the relationship between their colours, trace element composition, micro-textures, and solid inclusions. It should be noted that the PPB sapphires represent a unique study case on the Andean continental margin due to the presence of their primary deposit developed in a geological context that is incompatible with this type of formation.

Geological setting

The PPB area is located 45 km NE of the capital city of Copiapó in the Atacama region, Chile (Fig. 1a–b). The Jurassic volcano-clastic La Negra Formation, Cretaceous La Brea and the La Borracha plutons represent the most important geological units of this area, which are almost entirely covered by Quaternary non-consolidated sediments (Fig. 1b–c) (Arévalo 2005). The area is cross-cut by the Atacama Fault System (AFS) (Fig. 1b), which corresponds to an active structural system with an extension of at least 1000 km within the Cordillera de la Costa of the Central Andes in Chile and is described as an N–S sinistral strike-slip fault system that was active from Early Cretaceous (Arabasz 1971; Brown et al. 1993; Grocott et al. 1994). This sapphire-rich deposit was formed because of contact metasomatic de-silicification between granodiorites from La Brea Pluton and basaltic lavas from La Negra Formation through the AFS. The sapphire-rich metasomatites extend over a superficial area of $\sim 1070 \text{ m}^2$, which are characterised by six lithological units with different amounts of corundum, sillimanite, diaspore, böhmite, tourmaline and alunite (Miranda-Díaz et al. 2022) (Fig. 1c).

Methodology

Approximately 60 kg of non-consolidated sediments were collected from three sampling sites surrounding the primary corundum-bearing deposit. To collect the samples, it was necessary to excavate holes about 0.5 m deep at each site. In-situ hand sieves with a pore size of 11.2 mm were used to sieve all samples initially, followed by a subsequent pore size of 4.75 mm to select grains under 4.75 mm. The grains

that met the criteria were further sieved by a stackable automatic riddle screen Retsch AS200 to obtain three different sizes, and sand samples between 3.35 mm and 1 mm in grain size were selected for further analysis. The JIG density separator was then used to obtain corundum-rich sands from each excavation. The corundum-rich sands were mixed and divided into quartets, resulting in 594 well-preserved corundum crystals that were weighed and photographed for recording. A Motic SMZ-168TL binocular lens coupled with a Motic-10 camera was used to classify the crystals by colour distribution. All these analyses were carried out at Universidad de Atacama, Chile.

Based on their physical properties, 77 representative crystals (Online Resource 1) were embedded in six epoxy resin mounts, each with a polished surface of their basal face (perpendicular to their *c*-axis). This process took place at the Fission-Track lab Freiberg (FTLF) at the Technische Universität Bergakademie Freiberg (TU-BAF) in Germany. A Zeiss confocal laser scanning polarised microscope LSM 800 with processing software imager. Z2m was used to obtain multi-focus photographs through the sapphires' *z*-axis. All samples were analysed at the Bioscience Institute at the TU-BAF.

JEOL JSM-6400 with Oxford Mono CL (SEM-CL) with a photomultiplier tube (PTM) was used to determine the sapphires' internal micro-textures. The system was usually operated at 15 kV accelerating voltage and 0.6 nA electron beam currents for CL imaging. The OM-CL measurements were carried out utilising a “hot cathode” cathodoluminescence microscope HC1-LM on thin polished sections that were coated with carbon (as described in Neuser et al. 1995) at the Mineralogy Institute at TU-BAF. The operational parameters for the system were set to an accelerating voltage of 14 kV and a current of 0.2 mA, which corresponded to a current density of approximately $10 \mu\text{A}/\text{mm}^2$. Luminescence images were captured “online” during CL operations using a Peltier-cooled digital video camera (OLYMPUS DP72). Cathodoluminescence spectra within the 370–1000 nm wavelength range were acquired using an Acton Research SP-2356 digital triple-grating spectrograph. A Princeton Spec-10 CCD detector was coupled to the cathodoluminescence microscope through a silica-glass fibre guide. CL spectra were measured under standardised conditions, which included wavelength calibration by a Hg-halogen lamp, a spot width of 30 μm , and a measuring time of 1 s. Due to sample preparation types, the 77 single sapphires mounted in resin from the secondary deposits were analysed only with SEM-CL. In contrast, sapphires from the primary lithological units (sapphire-bearing metasomatites) mounted in 7 representative thin sections were analysed in SEM-CL and OM-CL, totalling 76 analyses (Online Resource 2 and 3).

The first instrument used to acquire Raman spectra of solid inclusions is a TriVista spectrometer (Princeton Instruments; spectroscopy & Imaging) at the Institute of

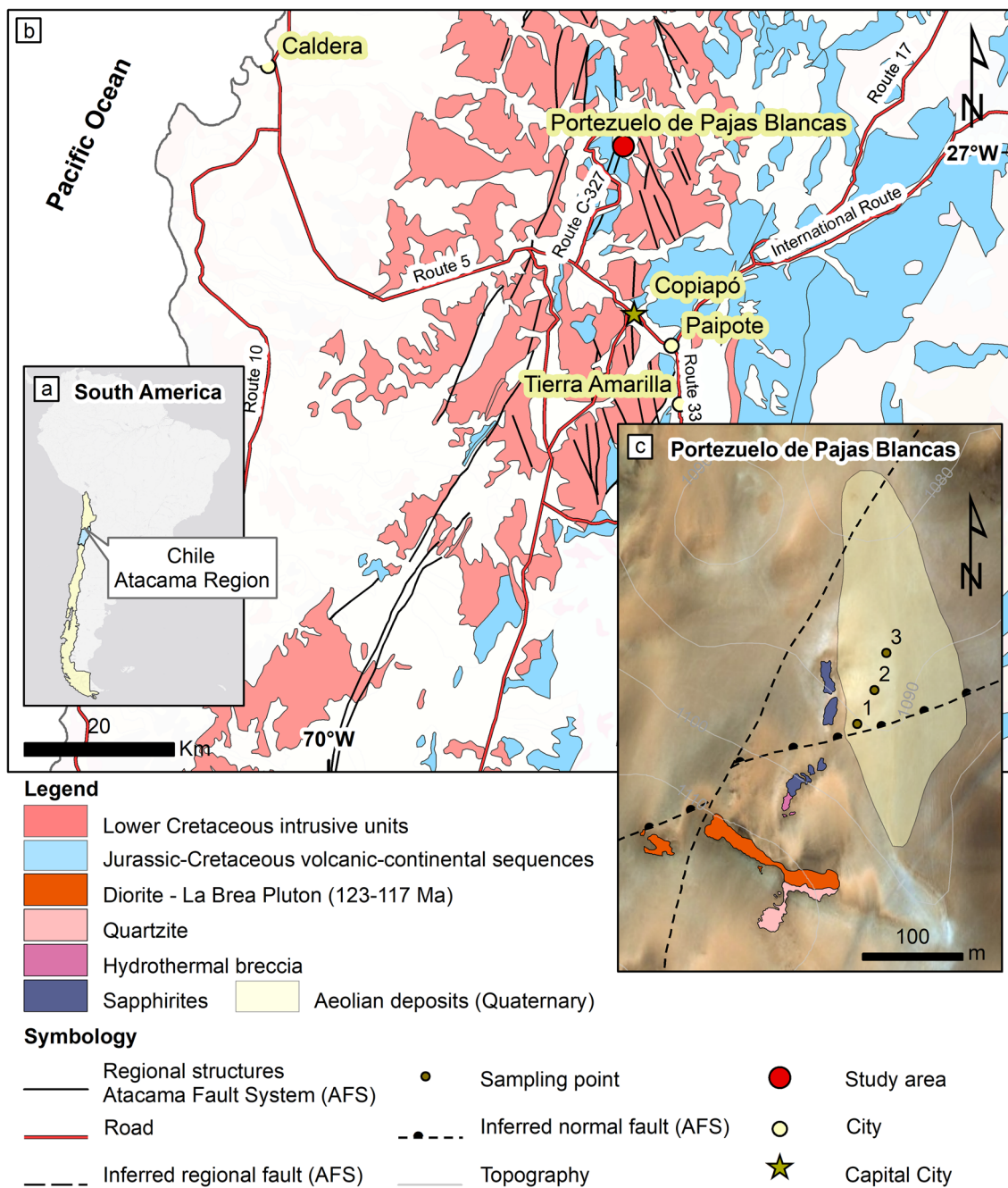


Fig. 1 Geological and location maps of the study area. (a) The Portezuelo de Pajas Blancas area (PPB) is in the Atacama region, northern Chile. (b) The regional map shows the study area, its access, main cities, study area and the regional geological/structural setting, in which the Lower Cretaceous intrusives, Jurassic-Cretaceous volcanic-

continental sequences, and the Atacama Fault System (AFS) are remarkable. (c) The local map displays the primary sapphire-bearing metasomatites and the secondary aeolian placer with their sampling points

Geology, TU-BAF. This instrument is connected to an Olympus BX51W1 microscope with a 100 (n. a. 0.75) objective and operated in single mode. The system uses a coherent Sapphire SF NX 488 nm laser, and the spectrometer is calibrated to the 219.2 cm⁻¹ sulphur, 520.7 cm⁻¹ silicon, and 1001.4 cm⁻¹ polystyrene bands. The spectra

were collected using a 1500 g/mm optical grating, resulting in a spectral resolution of about ~4 cm⁻¹ with a pixel resolution of ~0.5 cm⁻¹ and a wavenumber range from ~160 to 1010 cm⁻¹. The measurements comprised 5 to 10 acquisitions of 10 s, with a 1–2 μm in diameter spot size.

The second instrument used in the study is the WiTec Confocal Raman Imaging System at the Institute of Glass Science and Technology, TU-BAF. This system comprises a UHT spectrometer, which operates a CCD camera detector, and an alpha 300 R Raman imaging microscope equipped with Olympus 20× and 100× objectives. The samples were excited with a coherent 532 nm Nd:YAG laser. Calibration and performance have been verified by checking the positions of the 520 cm⁻¹ line of a pure 001-oriented Si wafer and the Rayleigh line at 0 cm⁻¹. Calibration is regularly monitored using, i.e. the diamond 1332 cm⁻¹ line. The spectra were collected using a 1200 g/mm grating, with a pixel resolution of 1.9 cm⁻¹ and a range from around 13 to 1974 cm⁻¹, where the fingerprinting spectral features of the investigated minerals are located. The measurements consisted of 3 to 10 acquisitions, each lasting 3 to 5 s with a spot size ranging from 0.5 to 1 μm in diameter.

These crystals were also analysed using the Bruker M4 Tornado micro X-ray fluorescence (Micro-XRF) housed at Bruker Nano Analytics GmbH (Berlin, Germany) to determine the sapphires' elemental distribution. The system was operated at a tube voltage of 35 kV, an anode current of 800 μA, a pulse throughput of 275 kcps, and a vacuum of 2 mbar. The micro-XRF uses a Rh tube with a fixed focal point spot size of 20 μm. Measurements were made at various pixel spacings of 5, 10 or 20 μm. In addition, an Al 100 μm filter was used to remove potential diffraction peaks in the low kV range that could overlap with key elements of interest, e.g. Ti, Cr, Mn, and Fe specifically. Detection limits of the aforementioned elements are commonly around single-digit ppm levels in a sapphire matrix, but this depends on time per pixel. Pixel time varied but was commonly 20, 50 or 100 ms per pixel. Standardless quantification was based on the Fundamental Parameters approach described in Sherman (1955).

Results

The discovery and study of the PPB secondary sapphire-bearing aeolian placer deposit, in combination with previous studies of the PPB primary metasomatic deposit, have allowed for in-depth analysis of sapphires, determining that they possess different properties as sizes, colours, colour distributions, micro-textures, dislocations, inclusions, trace element concentration and distribution, which are described below (Online Resource 4).

Mineralogy of sapphires from the PPB primary metasomatic deposit

The sapphires present in the PPB metasomatites differ in abundance, size, and colour according to the different lithologies described previously by Miranda-Díaz et al. (2022) (Table 1). The homogeneously coloured sapphires occur in the sapphirite unit as granoblastic aggregates (Fig. 2a). In the diasporite as relics from alteration that formed the diasporite fibres (Fig. 2b). In the case of multi-coloured sapphires, these are found in the sapphire-dravite unit as euhedral aggregates, wherein the colours are symmetrically distributed across the crystals (Fig. 2c), whereas, in the böhmite-alunite-sapphire units, the sapphires are corroded and/or fractured, in which the colours are randomly distributed (Fig. 2d–e).

Mineralogy of sapphires from the PPB secondary aeolian placer deposit

The desertic aeolian placer deposit is located a few metres from the primary metasomatic deposit. It mainly consists of non-consolidated sands related to Quaternary non-consolidated dune fields (Fig. 1). In this placer deposit, the concentration of sapphire crystals is lower than 5 vol. %. In contrast, ~90 vol. % corresponds to silicate minerals (e.g. plagioclase and quartz), and ~5 vol. % consists of magnetite, hematite, and rutile. Sapphire crystals display various colours: (i) dark blue, (ii) blue, and

Table 1 Summary of the main mineral associations, sapphire abundance, and average sizes in each sapphire-bearing metasomatite at Portezuelo de Pajas Blancas, according to Miranda-Díaz et al. (2022)

PPB Metasomatites	Mineral association	Sapphire abundance	Sapphire sizes (mm)	Sapphire colours
Sapphirite	Crn, Dsp, Drv, Crn	> 90	0.19–1.4	DB, B, LB
Diasporite	Crn, Dsp, Drv, Cal	4	~0.1	DB, B
Sapphire-dravite	Crn, Drv, Tur	50	0.03–2.2	B, C
Red böhmite-alunite-sapphire	Bhm, Alu, Crn, And	70	0.1–2.6	DB, B, C
White böhmite-alunite-sapphire	Bhm, Alu, Crn, And	10	0.05–1.0	B, LB, C

DB Dark Blue, LB Light Blue, B Blue, C Colourless. Crn Corundum, Dsp Diasporite, Drv Dravite, Cal Calcite; Tur Tourmaline, Bhm Böhmite, Alu Alunite, And Andalusite.

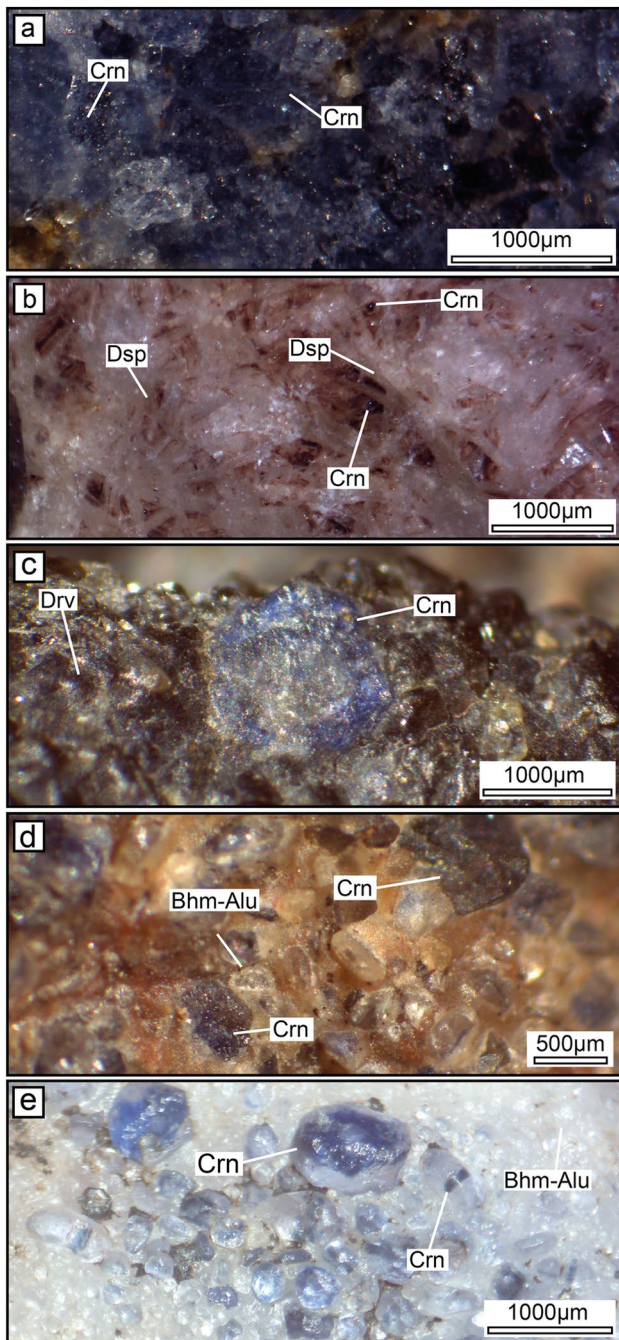


Fig. 2 Sapphires in the different PPB metasomatites. **(a)** *Sapphirite* displays granoblastic sapphires, which are mainly blue and colourless. **(b)** *Diasporite* shows sapphire relics immersed in diasporite fibrous. **(c)** *Dravite-sapphire metasomatite* displays euhedral multi-coloured sapphire. **(d–e)** *Böhmite-alunite metasomatites* display irregular multi-coloured sapphires immersed in böhmite-alunite groundmass

(iii) light blue, whereas some crystals are (iv) colourless (Fig. 3a). The crystals show a relationship between sizes and colours, where the largest sapphires are dark blue and blue, whereas the smallest sapphires are light blue and

colourless. The sapphires generally display a distinctive mixture and spatial distribution of colours. It is also possible to classify the crystals into six main types: type I: homogeneous, which consists of single-coloured crystals (Fig. 3a); type II: hourglass, in which the colour develops along the z-axis, forming an hourglass (Fig. 3b); type III: coloured core, in which the colour develops homogeneously along the z-axis, forming a cylinder (Fig. 3c); type IV and V: one- or two-coloured layers perpendicular to the z-axis (Fig. 3d–e); type VI: coloured zoning, wherein it is possible to distinguish the growth zoning due to colour differences (Fig. 3f); type VII: Irregular, in which an uneven mixture of colours presents gradations and distribution unrelated to their crystallographic axes. (Fig. 3g) The transitions between colours are generally abrupt in all sapphires except in types IV, V, and VII, where changes are gradual (Fig. 3d, e and g). Concerning the abundance, the colour distribution type I and the dark-blue sapphires are the most common crystal types (Table 2).

Sapphires micro-textures by SEM-CL

The sapphires display a mix of internal structures revealed by their cathodoluminescence properties, which were classified based on Götze et al. (2013), where primary textures are related to crystallisation and secondary textures to alteration, micro brecciation or re-crystallisation processes. Most sapphires show primary growth textures consisting of progressive and oscillatory zoning. Progressive zoning or primary growth zoning is characterised by variations in luminescence along the zonation, ranging from lower to higher intensity or vice versa. In contrast, oscillatory zoning consists of repeating or alternating variations of luminescence (Fig. 4a–c). Most of the crystals display a mixture of progressive and oscillatory zoning, which generally starts symmetrically from well-defined cores, wherein the thickness of the different zonation ranges from ~ 10 to 50 µm. Some sapphires display primary growth textures in combination with star-like textures in their basal face perpendicular to the c-axis, which have a relationship with the differential growth in the crystallographic axis (Fig. 4d–f).

Some sapphires also show secondary textures that overprint the primary growth textures described above. The micro-brecciation is related to sapphire fragments ranging in size from ~ 500 to 1000 µm, which generally have angular edges, although in some cases, the edges are rounded because of dissolution. The re-arrangement is associated with the brecciation, where the fragments are translated and rotated. The sapphire #568 (Fig. 4g–i) displays all the secondary alteration features described above.

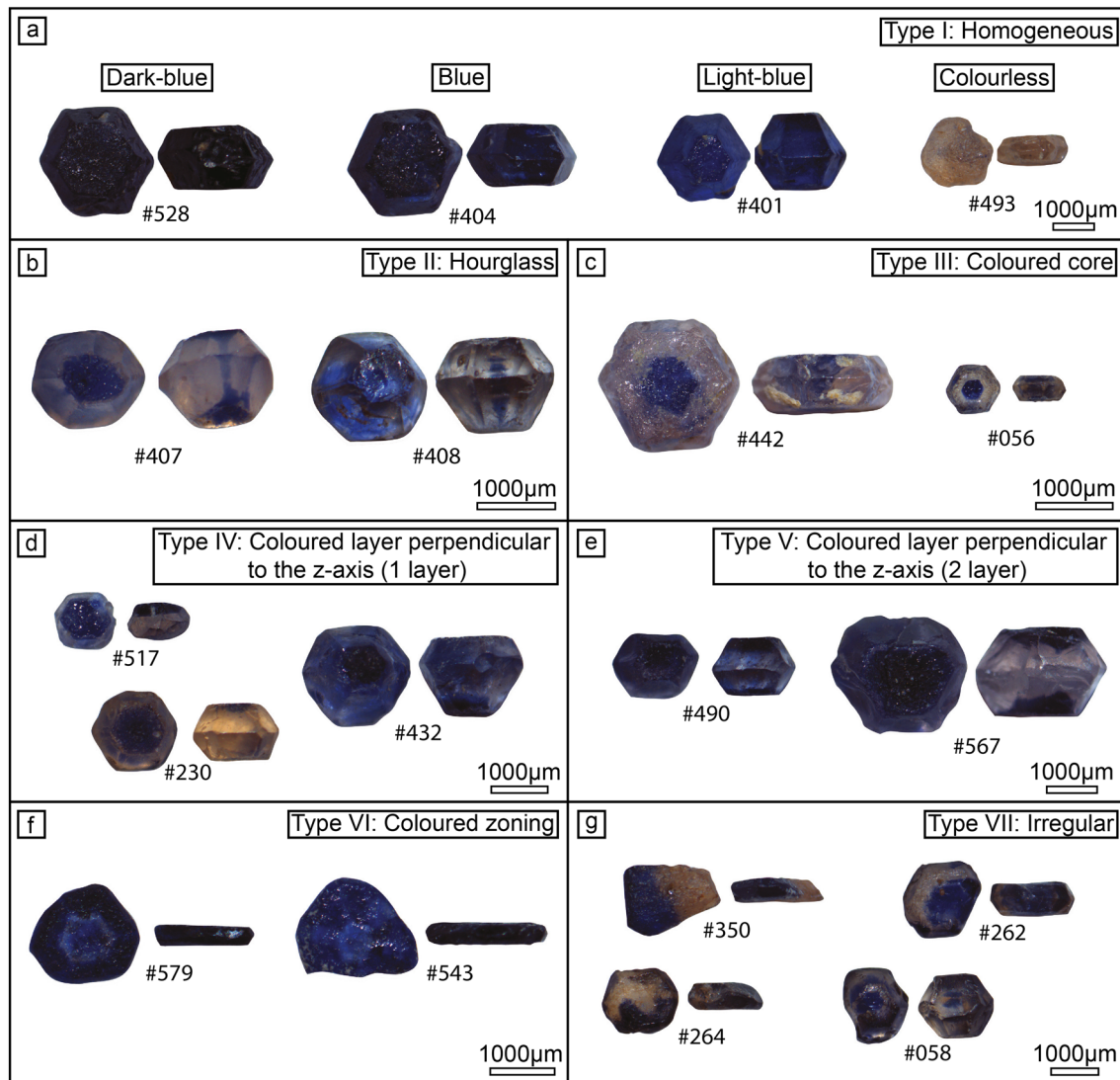


Fig. 3 PPB sapphire classification according to their colour distribution. **(a)** *Type I (Homogeneous)*: Single-coloured sapphires. **(b)** *Type II (Hourglass)*: Sapphires with coloured hourglass with the long axis parallel to the *z*-axis and the rest colourless. **(c)** *Type III (Coloured core)*: Sapphires with a coloured core or cylinder with its long axis parallel to the *z*-axis and the rest colourless. **(d–e)** *Type IV and type V (Coloured layers perpendicular to the *z*-axis)*: Sapphires with one- or

two-coloured layers perpendicular to the *z*-axis and the rest colourless. **(f)** *Type VI (Coloured zoning)*: Multi-coloured sapphires related to the growing zonation or unusual symmetrical colour distribution. **(g)** *Type VII (Irregular)*: Sapphires with an uneven mixture of colours, presenting gradations and distributions unrelated to their crystallographic axes

Sapphires micro-textures by OM-CL

The sapphires analysed by OM-CL correspond to samples from the primary metasomatic deposit. These sapphires show variations in their crystalline development, size and cathodoluminescence signal according to their host lithological units.

Specifically, the sapphires from the red-böhmite-alunite-sapphire metasomatite show a well-developed core with a progressive zoning rim. The red CL colour is related to the cores and, in some cases, to irregular

external zones, whereas the blue CL colour is associated with oscillatory zoning (Fig. 5a–b). In the sapphire-dravite metasomatite, the sapphires show dissolution and recrystallisation textures, where the red CL is predominant, and the blue CL only occurs in a few zones (Fig. 5c–d). In the white-böhmite-alunite-sapphire metasomatite, the sapphires show an outer quenched non-continuous rim, whereas the red CL colours are associated with the rest of the crystal (Fig. 5e–f). In the sapphire-rich metasomatite, the sapphires mainly display irregular red CL zones and a few irregular zones with blue to turquoise CL colours

Table 2 Sapphire abundance from the PPB area

	Quantity	%	Average weight (g)	Average weight (ct)
Colour predominance				
Dark-blue	239	40.2	0.018	0.092
Blue	195	32.8	0.012	0.061
Light-blue	85	14.3	0.006	0.030
Colourless	75	12.6	0.007	0.037
Total	594	100		
Sapphire colour distribution				
Type I: Homogeneous	303	51	0.016	0.090
Type II: Hourglass	15	2.5	0.009	0.068
Type III: Coloured core	64	10.8	0.011	0.031
Type IV and V: Coloured layers	136	22.9	0.010	0.039
Type VI: Coloured zoning	21	3.5	0.005	0.017
Type VII: Irregular	55	9.3	0.013	0.062
Total	594	100		

The representative population of sapphires (594) is expressed in colour predominance and colour distribution, where the average weights are shown in grammes (g) and carats (ct).

(Fig. 5g–j). In the diasporite, the sapphires display homogeneous red CL (Fig. 5k–l).

Inclusion mineralogy by Raman and micro-XRF analyses

Three types of mineral inclusions were identified in the sapphire crystals: andalusite, rutile, and anhydrite, which show different shapes, diameters, and relative abundance amongst the sapphires, which are summarised in Table 3 and Online Resource 5. The andalusite inclusions showed bands at a Raman shift of 290, 320, 358, 918 and 1065 cm^{-1} (Fig. 6a). The micro-XRF elemental distribution maps confirm the presence of Si, which is consistent with the andalusite inclusions (Fig. 7a–d). These inclusions are characterised by their euhedral crystalline development and lack of dissolution or alteration at the edges. The size range of crystals varies from ~50 to ~553 μm , with no preferential orientation concerning the host crystal.

Rutile inclusions showed Raman bands at 142, 245, 441, 608 and 918 cm^{-1} (Fig. 6b). The micro-XRF elemental distribution maps confirm the occurrence of Ti in the zones where rutile inclusions are found (Fig. 7e–l). These inclusions can occur as tiny anhedral crystals with honey-coloured shades distributed in clusters, ranging from ~22 to ~79 μm . Rutile inclusions also occur as large euhedral crystals with honey-coloured shades, ranging from ~104 to ~219 μm . These inclusions can also occur as subhedral fibrous colourless crystals, which are homogeneously

distributed, creating a silk-like appearance with sizes varying from ~170 to ~606 μm .

The anhydrite inclusions showed Raman bands at 167, 497, 626, 674, 1015, 1127 and 1158 cm^{-1} (Fig. 6c) and are characterised by their rounded shape that can be divided into two types. The first group corresponds to isolated anhedral inclusions, ranging in size from ~49 to ~812 μm , which generally exhibit one or two cleavage sets. The second group is related to anhedral inclusions, which always occur in clusters, where the size range of crystals varies from ~21 to ~593 μm . The micro-XRF detection of elements of surface inclusions in both types of anhydrites confirms the presence of S and Ca (Fig. 7m–p).

In addition, dislocations related to solid inclusions showing elongated and sectioned tube-shaped forms were detected in some sapphires, which have lengths of up to 350 μm and widths of around 15 μm . These dislocations occur in sapphires with strong colour variations, which host several inclusions (Online Resources 5).

Trace elements geochemistry of sapphire crystals

Micro-XRF results reveal that the main trace elements on sapphires from the PPB correspond to Fe and Ti, which are always over the detection limits and present in practically all sapphires, varying in distribution and concentration across the different primary micro textures and secondary alteration features. For example, it is possible to find variations of these elements in accordance with crystallographic axes (Fig. 8a–c), in cores or external rims related to growth textures (Fig. 8d–f), and in higher concentrations in the outer rim than in the core (Fig. 8g–i). Cr traces are generally associated with crystal cores or, in some cases, at the crystal boundaries, whereas Ga is below the detection limit of micro-XRF, but trace amounts have been reported by LA-ICP-MS analyses (Miranda-Díaz 2024).

Discussion

Correlation between the sapphires from the metasomatic deposit and the aeolian placer deposit

Based on all available information, it is confirmed that the sapphires found in the aeolian placer deposit are from the metasomatic deposit. Although evident because of their proximity, this is confirmed mainly by the sapphire sizes, micro-textures, and colours (Table 4). The sapphirite and diasporite metasomatic units display sapphires Type I, and the sapphire-dravite metasomatite show sapphires type II, III, IV, and V, confirming that these metasomatic units have formed mainly in the first, second and early third

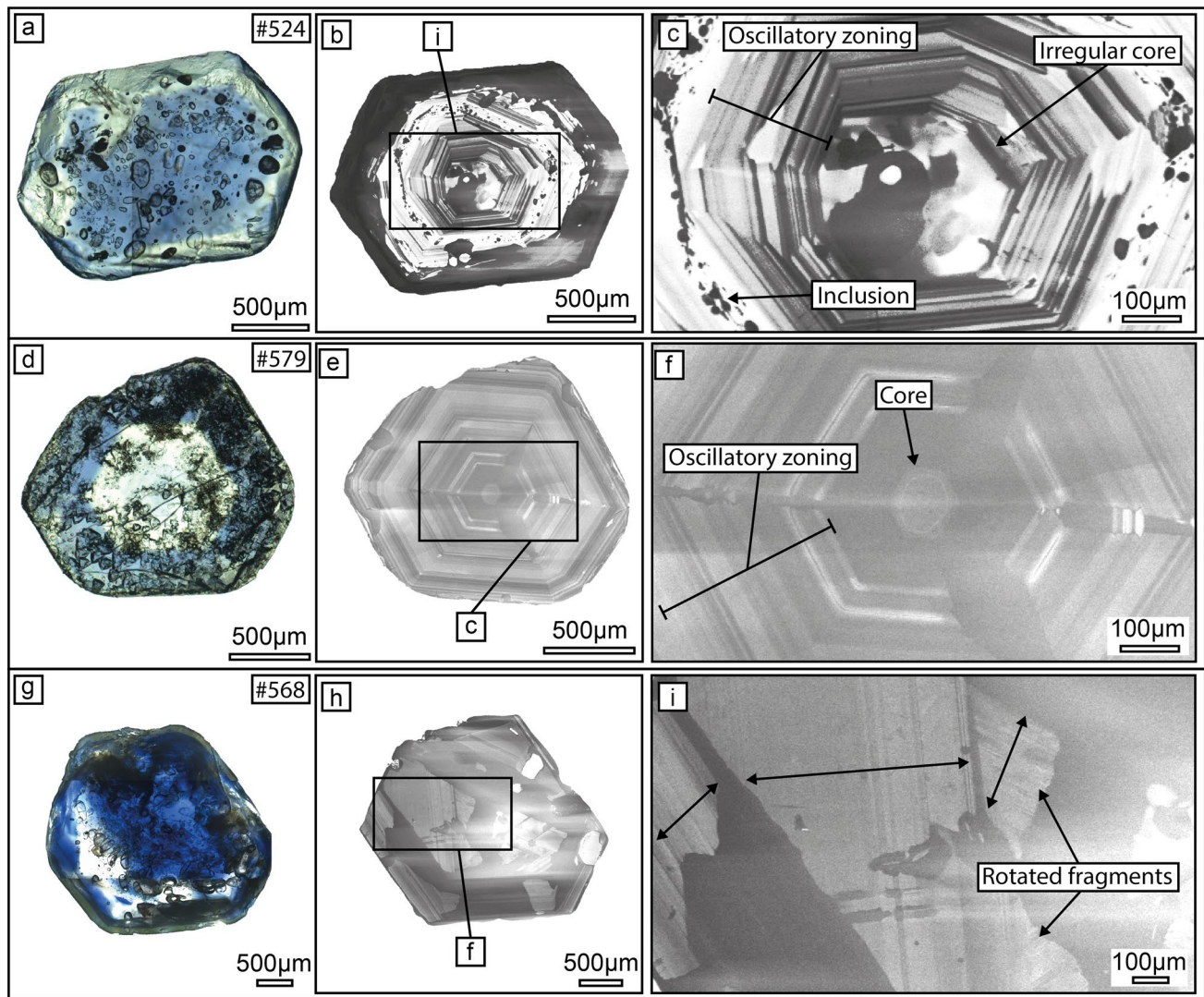


Fig. 4 SEM-CL and multi-focus transmitted-light photograph analyses of basal sections of representative sapphires. **(a–c)** *Sapphire #524 (Type III)*. **(a)** Multi-focus transmitted-light photograph displaying light-blue sapphire with an irregular colourless rim and several solid inclusions. **(b)** Irregular core and inner rim with oscillatory and progressive zoning, and irregular outer rim. **(c)** Irregular core and inner rim. The inner rim displays oscillatory and progressive zoning. **(d–f)** *Sapphire #579 (Type IV)*. **(d)** Multi-focus transmitted-light photograph that displays a colourless core and blue rim. **(e)** Sapphire with progressive and oscillatory zoning. The edge of the crystal shows dis-

solution and re-crystallisation. **(f)** Regular core and oscillating rim of the sapphire. It should be noted that this specimen shows differential growth related to crystal symmetry (star-like). **(g–i)** *Sapphire #568 (Type VII)*. **(g)** Multi-focus transmitted-light photograph of blue sapphire displaying colourless zones and several solid inclusions **(h)** Micro-brecciation and re-arrangement of fragments, together with progressive zoning. **(i)** Fragments with irregular edges and progressive zoning. The double arrows indicate the direction of the fragments' growth

formation stages. The böhmite–alunite–sapphire metasomatites show sapphires type VII, which is related to the fourth and fifth formation stages. The different types of sapphires and their relation to the different metasomatic units confirm the anisotropic character of formation.

Relationship between crystal chemistry, cathodoluminescence and colours

The occurrence of cathodoluminescence depends on several factors (e.g. activators, sensitiser, and quenchers), so

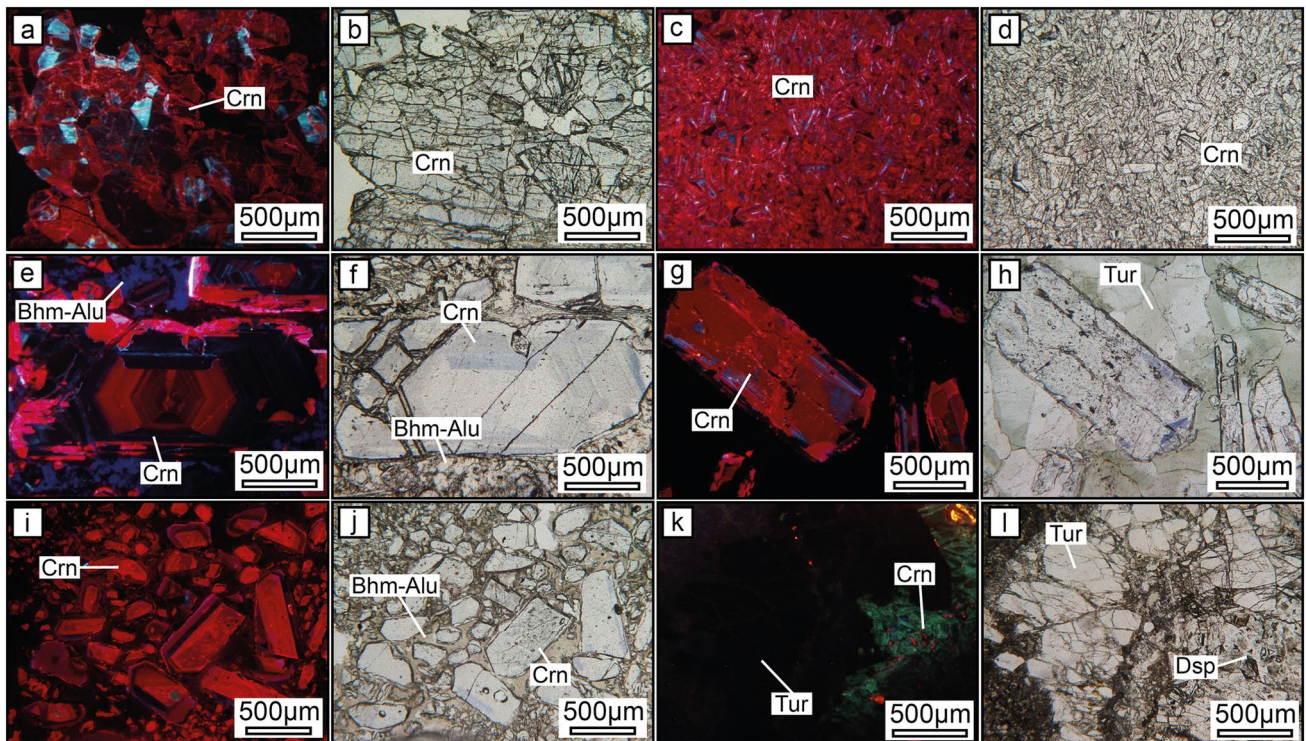


Fig. 5 Optical microscope cathodoluminescence (OM-CL) analysis and photomicrographs of sapphire-rich metasomatites. (a–d) Granoblastic sapphires from *sapphirite* display red CL, except in some areas showing a turquoise luminescence. (e–f) Euhedral sapphire from *böhmite-alunite-sapphire metasomatite*. The sapphire displays an irregular red core with progressive and oscillatory blue zoning. There are irregular red areas on the edges of the crystal due

to the dissolution and re-crystallisation. (g–h) Euhedral sapphire from *dravite-sapphire metasomatite* shows mainly red CL, and some areas show blue CL. (i–j) Euhedral to anhedral sapphires from *böhmite-alunite-sapphire metasomatite* display mainly red CL and a discontinuous quenched rim. (k–l) Anhedral sapphires from *diasporite*, which shows red luminescence immersed in fibrous euhedral diaspores

Table 3 The number and percentage of sapphires possessing solid inclusions, dislocations and microtextures

	N° sapphires	%
Solid inclusions		
Andalusite	27	35.1
Rutile	56	72.7
Primary anhydrite	55	71.4
Secondary anhydrite	53	68.8
Dislocations		
Tube-like voids	13	16.9
Primary micro-textures		
Core developed	33	42.9
Primary growth zoning	45	58.4
Oscillatory zoning	22	28.6
Sector zoning	42	54.5
Secondary micro-textures		
Brecciation and re-arrangement	35	45.5
Dissolution	48	62.3

establishing quantitative correlations of luminescence signal and single causes is often impossible (Remond et al. 2000; Kempe and Götze 2002; Götze et al. 2013). Amongst the qualitative correlations of the PPB sapphires, the red CL emission is related to traces of Cr^{3+} and Ti^{3+} . In contrast, the blue CL emission is associated with Ti^{4+} (Fig. 9). These luminescence phenomena have been widely documented wherein Cr^{3+} in corundum activates double intense luminescence peaks generally at 692.8 nm and 694.3 nm (Chapoulie et al. 1999; Ponahlo 2000; Nasdala et al. 2004; Gugushev et al. 2010; Gaft et al. 2015), and the large band which is linked to Ti^{3+} between 728 and 794 nm (Chapoulie et al. 1999). Blue CL may be caused by a broad band of short-wave CL characterised by two peaks at 472 nm and 483 nm (Ponahlo 2000) related to Ti^{4+} , wherein the emission results from a charge transfer transition of the $[\text{Ti}^{4+}\text{O}_6]^{8-}$ complex (Blasse and Verweij 1990; Chapoulie et al. 1999). Fe^{2+} is one of the main luminescence quenchers (Marfunin 1979; Walker 1985; Chapoulie et al. 1999; Pagel et al. 2000; Yu and Clarke 2002; Gugushev et al. 2010; Giuliani et al. 2014), i.e. the Cr^{3+} emission in corundum is negatively affected by the presence of Fe (Nasdala et al. 2004; Giuliani

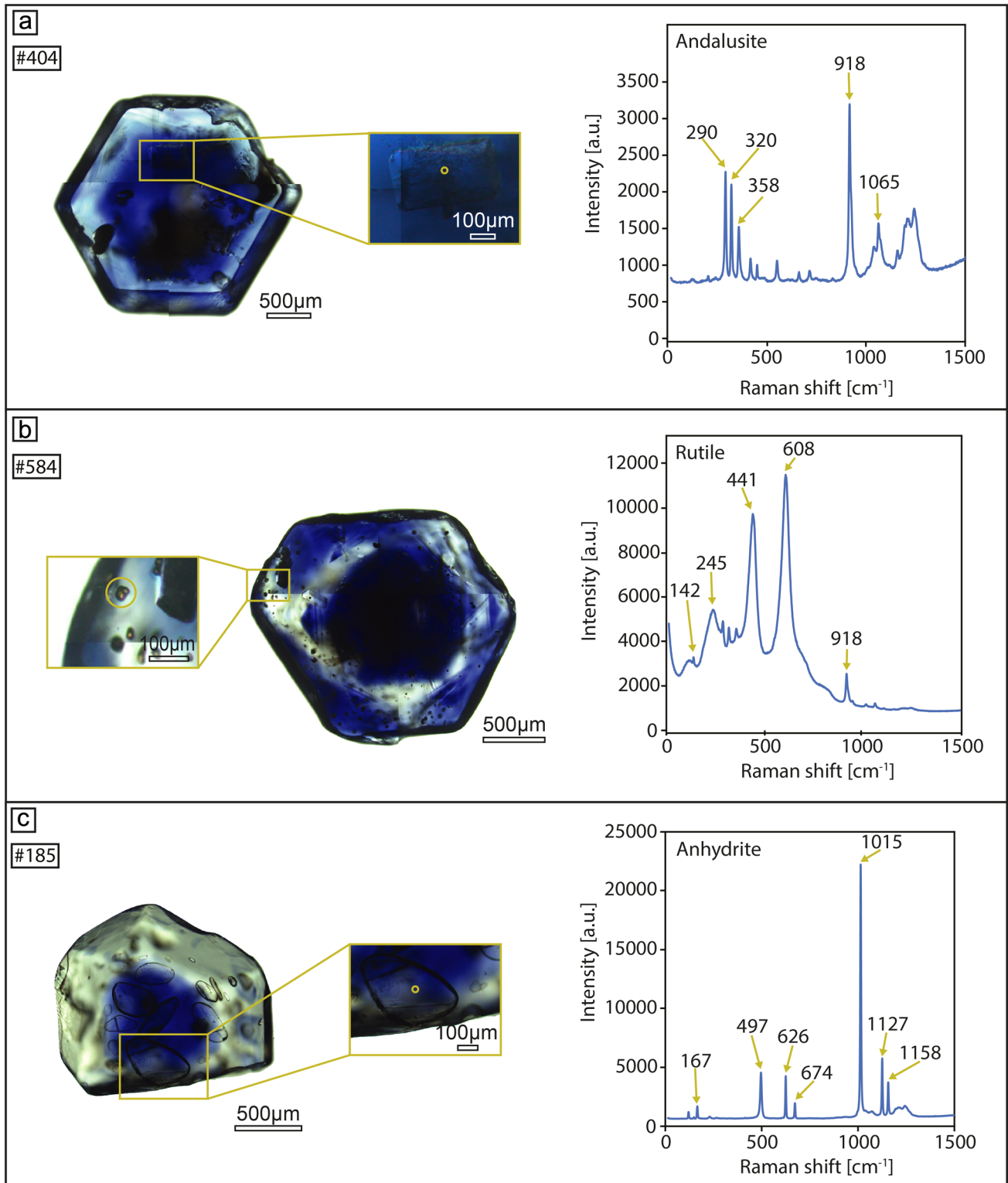


Fig. 6 Raman spectra of solid inclusions in sapphire with annotated main bands. **(a)** Euhedral andalusite inclusion in *sapphire* #404. **(b)** Anhedra rutile inclusion in *sapphire* #584. **(c)** Anhedra anhydrite inclusion in *sapphire* #185

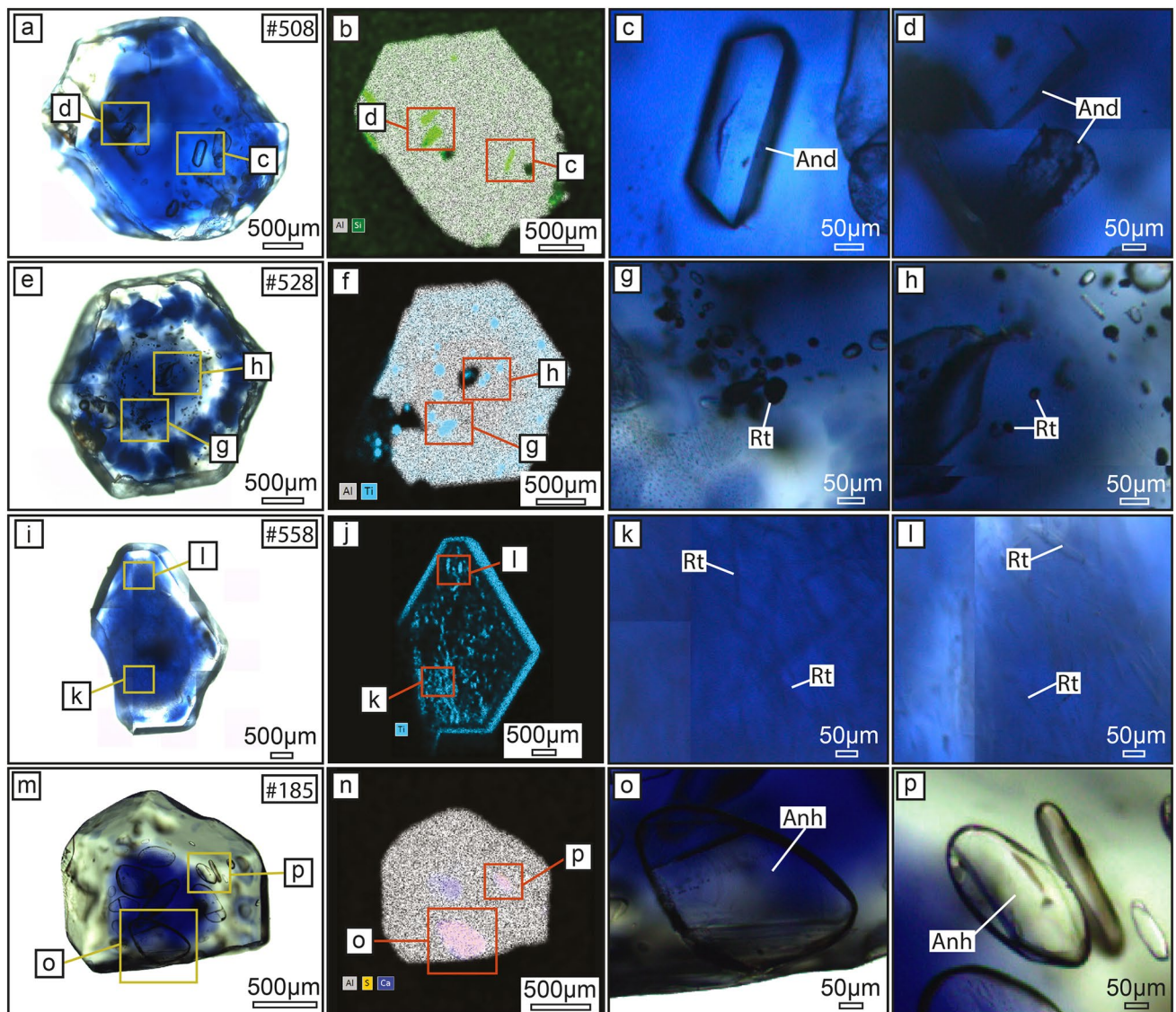


Fig. 7 Micro-XRF elemental data from inclusions within sapphires (**a–d**) *Sapphire #508*. (**a**) Multi-focus transmitted-light microphotograph. (**b**) Elemental distribution map of Si and Al. High-Si zones are related to andalusite inclusions. (**c–d**) Microphotograph of euhedral andalusite inclusions. (**e–h**) *Sapphire #528*. (**e**) Multi-focus transmitted-light microphotograph. (**f**) Elemental distribution map of Ti and Al. High intensities are due to rutile inclusions. (**g–h**) Anhedral rutile

inclusions. (**i–l**) *Sapphire #558*. (**i**) Multi-focus transmitted-light microphotograph. (**j**) Elemental distribution map of Ti. High intensities of Ti are related to silk rutile inclusions. (**k–l**) Subhedral silk rutile inclusions. (**m–p**) *Sapphire #185*. (**m**) Multi-focus transmitted-light microphotograph. (**n**) Elemental distribution map of Al, S, and Ca. High intensities of S and Ca are related to anhydrite inclusions. (**o–p**) Anhedral anhydrite

et al. 2014), so Fe-rich sapphires do not display luminescence at all (Ponahlo 2000) or only very weakly.

The PPB sapphires are generally multi-coloured, showing varieties of blue in combination with colourless zones. One of the main physical properties that make corundum a gemstone is its colour. In the case of sapphires, the generation of colour is mainly due to the presence of trace elements such as Fe, Ti, and Cr that replace Al in the crystal structure, acting as chromophores and generating the blue, yellow, and colourless varieties (Ferguson and Fielding 1971;

Nikolskaya et al. 1978; Fritsch and Rossman 1987, 1988; Peretti et al. 1996; Hughes 1997; Schmetzer et al. 1999; Rakotondrazafy et al. 2008; Bgasheva et al. 2012; Giuliani et al. 2014; Hughes et al. 2017; Giuliani and Groat 2019; Palke 2020; Pignatelli et al. 2020). Specifically, the colour is caused by these dispersed metal ions and the modification of their valence states (Fritsch and Rossman 1987). In the case of sapphires, the charge transfer $O^{2-}-Fe^{2+}$ absorption is centred in the ultraviolet, with minimal effect on colour, whereas the $O^{2-}-Fe^{3+}$ absorption is rather on the edge of

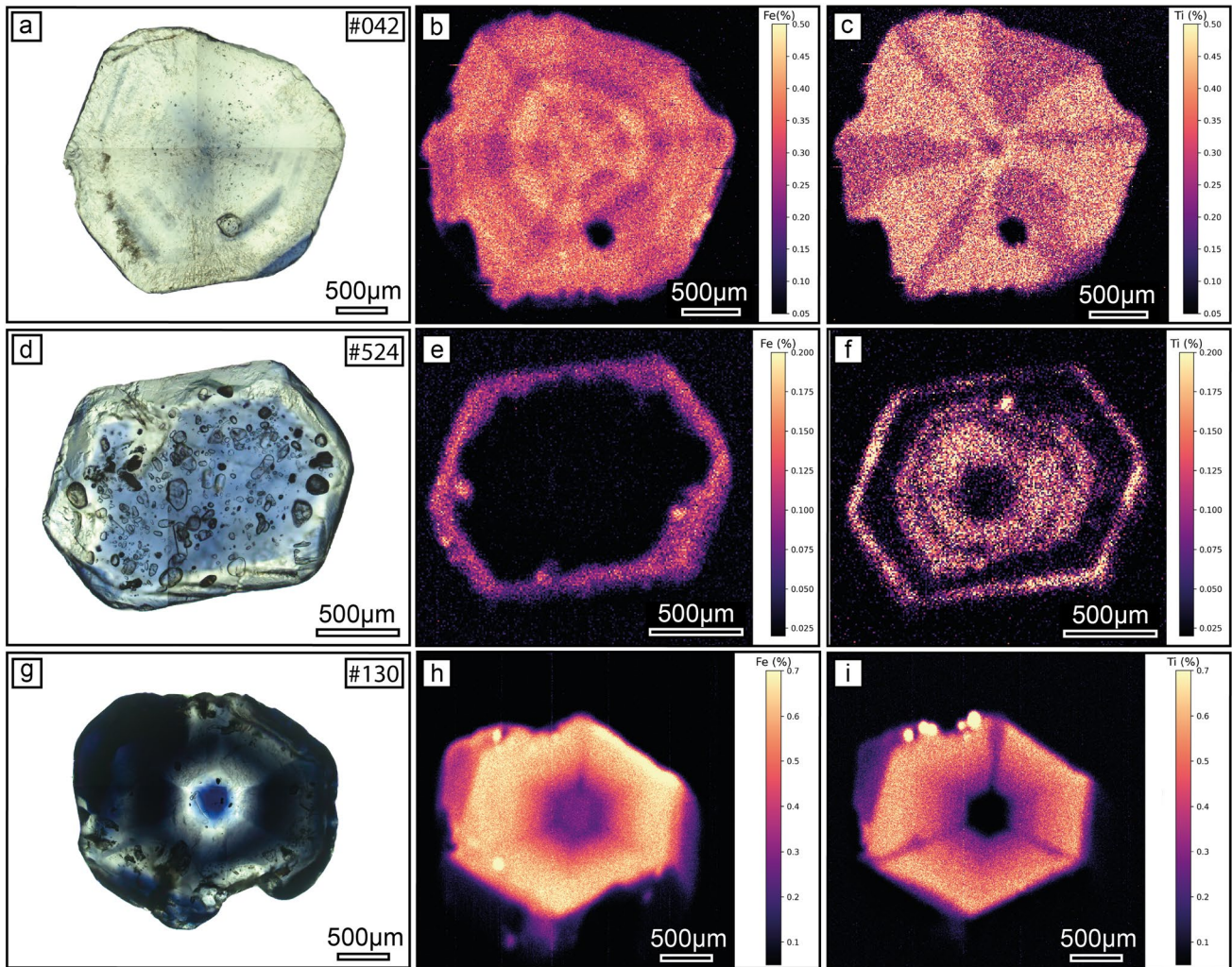


Fig. 8 Representative micro-XRF qualitative elemental distribution map of sapphires' basal sections. The concentration is expressed in wt%. **(a–c)** *Sapphire #042 (Type I)*. **(a)** Multi-focus transmitted-light photograph. **(b)** Fe distribution map showing oscillatory zoning. **(c)** Ti distribution map with star-like zoning. **(d–f)** *Sapphire #524*. **(d)** Multi-focus transmitted-light photograph. **(e)** Fe distribution map

related to the outer ring. **(f)** Ti distribution map showing core-rim zoning. **(g–i)** *Sapphire #130*. **(g)** Multi-focus transmitted-light photograph. **(h)** Fe distribution map display higher concentrations in the outer rim. **(i)** Distribution map display Ti concentration only in the outer rim

the ultraviolet wavelength range, causing yellow to brown shades (Fritsch and Rossman 1988; Bgasheva et al. 2012). The intervalence charge-transfer transition IVCT between

Table 4 Correlation between sapphire types and lithological units found in the metasomatic deposit

PPB metasomatites	Sapphire types
Sapphirite	I
Diasporite	I
Sapphire-dravite	II, III, IV, V
Red böhmite–alunite–sapphire	VII
White böhmite–alunite–sapphire	VII

$\text{Fe}^{2+}-\text{O}^{2-}-\text{Ti}^{4+}$ ions is the main factor in the generation of the blue colour in sapphires (Ferguson and Fielding 1971, 1972; Fritsch and Rossman 1988; Kane et al. 1990; Schmetzer and Kiefert 1990; Bgasheva et al. 2012; Giuliani et al. 2014). The IVCT has a probability of up to two orders of magnitude higher than other processes related to transition metal ions substituted in Al_2O_3 (Townsend 1968), such that less than 0.01% of Fe and Ti are sufficient to produce a blue colour in sapphires (Bgasheva et al. 2012; Giuliani et al. 2014). Isolated Ti^{4+} ions do not have any absorption bands in the visible region (Bgasheva et al. 2012). The intensity and generation of the colours depend not only on the concentration of these trace elements but also on their different valence state configurations, causing changes in the degree

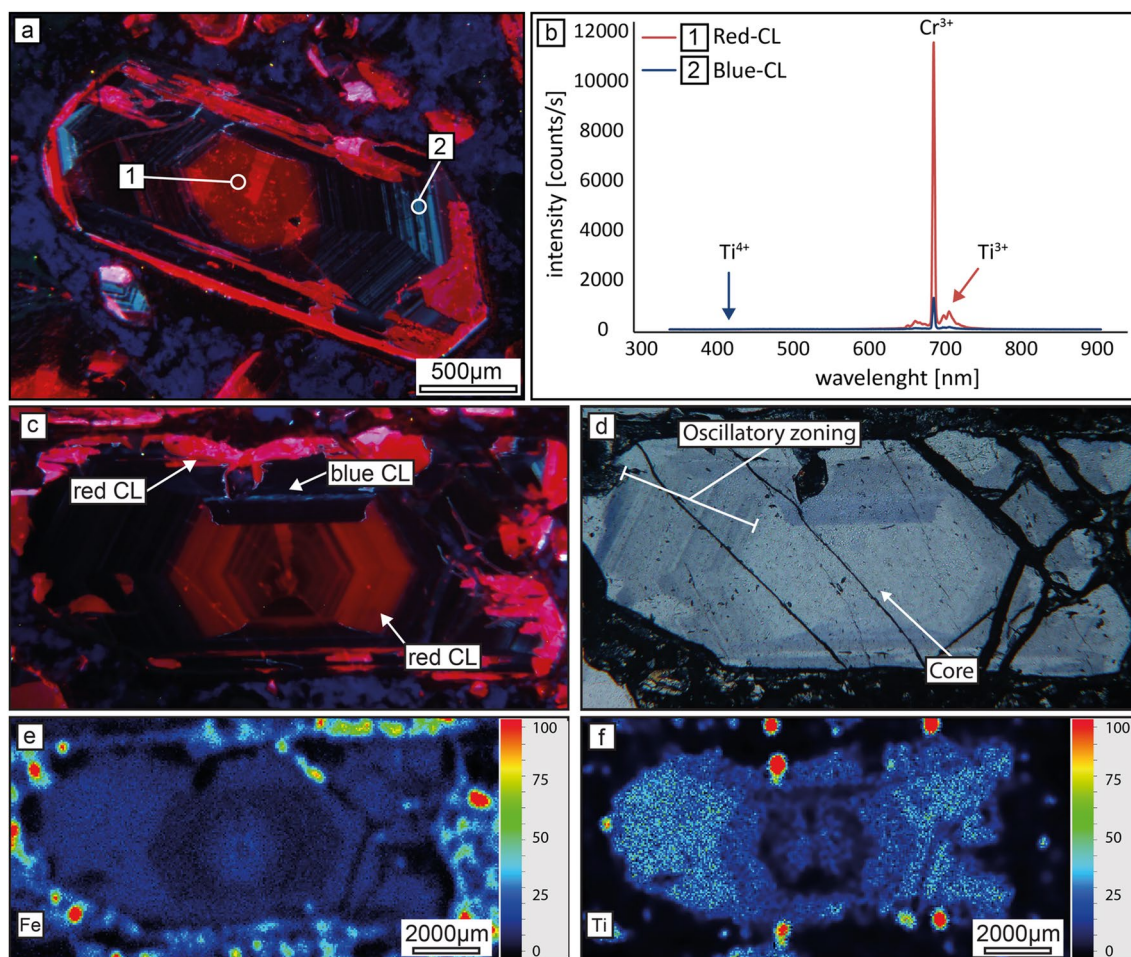


Fig. 9 OM-CL, Optical microscope microphotograph, and Micro-XRF elemental distribution maps of subhedral sapphire crystal from the böhmite-alunite-sapphire metasomatite. **(a)** OM-CL analysis of euhedral sapphire displays an irregular red core with progressive and oscillatory blue zoning. There are irregular red areas on the edges of the crystal due to the dissolution and re-crystallisation. **(b)** OM-CL spectra of the analysed points in **(a)**, wherein points 1 and 2 correspond to red and blue spectra, respectively. It should be noted that the

peaks confirm traces of Cr^{3+} , Ti^{3+} , and Ti^{4+} . **(c)** The OM-CL image displays red CL in the core and re-crystallisation zones at the crystal boundaries. The quenched zones indicate some blue CL. **(d)** Polarised optical microphotograph showing the oscillatory zoning and progressive zoning by pleochroism. **(e-f)** Fe-Ti elemental distribution maps display the variations of these elements through micro-textures, respectively

of absorption of IVCT in the visible part of the spectrum (Fritsch and Rossman 1988).

According to sapphires' CL signal, trace elements, and colour properties, some statements can be made. In the sapphires from the böhmite-alunite-sapphire metasomatite, a direct relationship exists between the colourless zones and the red CL. Firstly, the presence of Cr^{3+} and Ti^{3+} traces, combined with traces of Fe, cause absorption in the non-visible light spectrum, producing colourless sapphire. Secondly, the CL-quenched areas are related to Fe and Ti traces, implying that the IVCT of $\text{Fe}^{2+}-\text{O}^{2-}-\text{Ti}^{4+}$ may generate the blue colours, wherein Fe^{2+} is assumed to be the main CL-quencher (Fig. 9). Another example is the sapphires type II and III from the aeolian placer deposit, which displays blue-coloured cores with Ti and Cr traces,

wherein Cr^{3+} allows the micro-textures to be distinguished by its luminescence, and Ti^{3+} plays a role in the colour generation. Following this, the colourless rims show Fe, Ti, and Cr traces, which produce absorption in the non-visible light spectrum and quench the CL signal (Fig. 10). These different examples have shown that the development of colourless zones can occur despite trace elements such as Fe, Ti, and Cr, in which not only the concentration but also the valence state of these trace elements influences the type of bonding and, thus, the generation of colour in specific cases. It is proposed that these variations in colour, CL signal, and trace elements result from variations in forming conditions during sapphire development, allowing the definition of the main stage of formation.

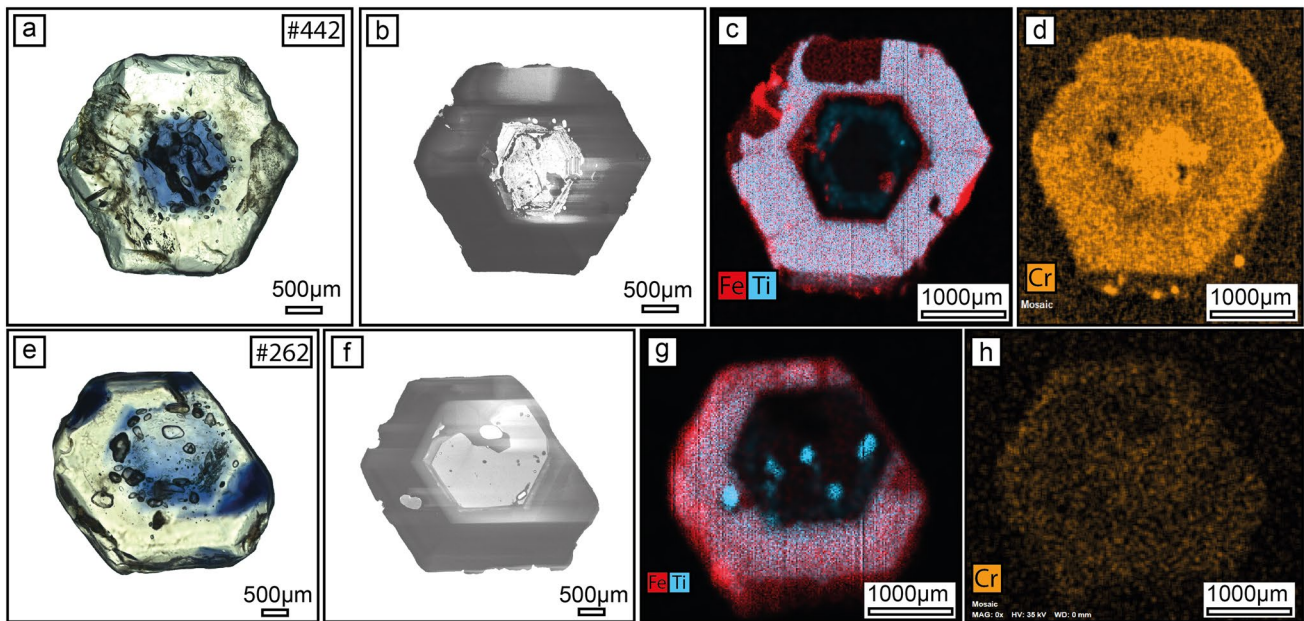


Fig. 10 SEM-CL micro-textures and Micro-XRF distribution maps of coloured core sapphires. **(a–d)** *Sapphire #442*. **(a)** Multi-focus transmitted-light photograph showing a light-blue core with several inclusions and a colourless rim **(b)** Irregular core and external homogeneous rim by SEM-CL. **(c)** The Fe-Ti distribution map shows an enriched rim. **(d)** The Cr distribution map shows concentration in the core and the outer rim. **(e–h)** *Sapphire #262*. **(e)** Multi-focus trans-

mitted-light photograph displaying an irregular light-blue core and a colourless outer rim. Note the presence of several inclusions in the boundaries between the core and rim. **(f)** Irregular core and rim by SEM-CL. **(g)** Fe-Ti distribution map shows an enriched rim. **(h)** Cr distribution map shows similar concentrations in the core and outer rims

Genetic implications of mineralogical and microtextural features of sapphires

One aspect that stands out in the primary and secondary PPB sapphires is their euhedral development. Barker (1998) states that euhedral crystals developed in metamorphic environments can be related to slow, unimpeded growth in a heterogeneous medium. The millimetre sizes of the sapphire crystals in PPB are related to the metasomatic forming conditions, which favour nucleation over crystal growth, i.e. the prograde rocks have a predominantly granoblastic texture, which indicates high physicochemical stability and is common in high-grade metamorphic systems (Barker 1998).

The micro-textures found in PBB sapphires show evidence of the processes involved during crystal formation. The crystals commonly display well-defined cores accompanied by layers (rims), which could be due to a multi-stage growth mechanism (Liu 2015; Pignatelli et al. 2020). The development of cores at the beginning of crystal growth can be considered the first formation stage, which can be homogeneous without inclusions because element inputs are constant and do not fluctuate (Barker 1998) or heterogeneous with several inclusions.

The second stage is associated with progressive and oscillatory zoning around the cores. Specifically, progressive zoning is due to the variation of available trace elements

and growth defects (Tracy 1982; Götze et al. 2013). These elements can form part of the newly developing layers due to various factors (e.g. diffusion of atoms to the crystal surface). However, this development only occurs when the bonds between the atoms attached to the crystal edge are stronger than the activation energy associated with the diffusion processes (Bard 1986). Oscillatory zoning is a widely studied phenomenon that can develop in a wide range of open-system environments (Yardley et al. 1991). For example, in a metamorphic environment, it can be interpreted as open-system behaviour (Barker 1998), as well as, the development of this texture in some solid solutions of metamorphic minerals such as garnets and pyroxenes from skarns is well known (Barker 1998). Oscillatory zoning is caused by the coupling between the kinetic energy of crystal growth and the elements in diffusion at the fluid-crystal interface (Allègre et al. 1981; Götze et al. 2013). One of the characteristics necessary to form this texture is a chemical imbalance and a feedback mechanism that changes the reaction rates in response to those taking place (Ortoleva et al. 1987; Yardley et al. 1991), as well as low crystal growth rates (Allègre et al. 1981), which indicates that as the sapphires grew and incorporated elements into their structure, successive metasomatic pulses incorporated new elements into the system.

The third stage includes the development of fractures and dissolution in sapphires, which affect the growth zoning of

crystals. Micro-brecciation occurs mainly in metamorphic environments due to variations in temperature and pressure conditions (e.g. tectonic deformations) (Götze et al. 2013). Bard (1986) states that low-temperature deformations ($T \leq 200$ °C) can produce catalases. However, these processes depend on the stress and strain rate, the mineral elasticity and its orientation concerning the principal stress, the temperature, and interstitial fluids (Bard 1986). Micro brecciation indicates increased differential stress in a brittle medium where the sapphires were fragmented and dissolved due to changed forming conditions.

The fourth stage is related to the re-arrangement of previously formed sapphire fragments, which were trapped and incorporated into new overgrowth sapphires. Finally, the fifth stage relates to Fe-Ti-Cr colourless irregular outer rim formation (e.g. sapphires from Fig. 10), related to changing conditions during the late formation stage. This phenomenon has been called diffusion zoning and is described in other metamorphic minerals (e.g. garnets), consisting mainly of the distribution of atoms in the crystal structure and relative changes in the atoms, where reabsorption depends on cooling and diffusion ratios (Barker 1998). The difference with growth zoning is that diffusion zoning develops in already formed crystals and is not necessarily homogeneous, as it is also driven by the reaction between the crystal surface and other elements in contact through an intergranular film or fluid (Tracy 1982). This texture can be interpreted as the product of multi-episode metasomatism, generating discontinuous zonation from resorption and overgrowth (Barker 1998).

A good example is sapphire #395 (Fig. 11), which shows all five formation stages, which are described below: the first stage consists of the development of a heterogeneous core; the second stage consists of progressive and oscillatory non-symmetrical zoning, where the light-blue dominates; the third stage is evident by micro-brecciation of the previously formed sapphire with rounded and irregular edges due to dissolution; the fourth stage consists in overgrowth and incorporation of previously formed fragments; finally, the fifth stage consists of the development of Fe-Ti enriched and colourless rims.

Genetic implications of solid inclusions and dislocations

The PPB sapphires have been considered metasomatic because of the relationship between the mineral textures and the contacts of the lithological units from the primary deposit (Miranda-Díaz et al. 2022). The study of solid inclusions confirmed the metasomatic origin in other sapphire deposits (Hughes et al. 2017), which tend to be deficient in primary fluid inclusions (Roedder and Patterson 1982). In the case of PPB sapphires, these are characterised by many

solid inclusions and the absence of fluid inclusions. Euhedral andalusite solid inclusions are primary because their euhedral development is only possible with sufficient space for growth before being trapped into sapphires. Andalusite is stable under low-pressure conditions and at variable temperatures contact metasomatism (Weill and Fyfe 1961; Newton 1966; Althaus 1967; Holdaway and Mukhopadhyay 1993; Clarke et al. 2005; Bradt 2008).

Anhydrite is the most abundant inclusion in PPB sapphires, which is more consistent with a metamorphic/metasomatic environment than an igneous (Carroll and Rutherford 1987). The larger anhydrite inclusions can be considered primary crystals, which could have been formed during the sapphire's crystallisation. In contrast, the groups of small anhydrite inclusions (Online Resource N° 5) are considered secondary because they are related to healed micro-fractures. The occurrence of anhydrite implies sulphur-rich magmatism (Luhr et al. 1984; Bernard et al. 1991; Streck and Dilles 1998; Barth and Dorais 2000; Parat et al. 2002; Audétat et al. 2004; Newton and Manning 2005), so it is direct evidence of high sulphate magmatism (Chambefort et al. 2008). It should be noted that sulphur solubility in magmatic-hydrothermal fluids increases with the temperature and the iron content (Carroll and Rutherford 1987; Baker and Rutherford 1996; Streck and Dilles 1998; Jugo et al. 2005; Chambefort et al. 2008), whereas anhydrite solubility decreases with increasing temperature at low pressures (Blounot and Dickson 1969; Newton and Manning 2005). The solubility increases with increasing pressure at constant temperature and salinity (Blounot and Dickson 1969). For example, the solubility of anhydrite in concentrated NaCl solutions at near-magmatic temperatures (> 750 °C) indicates that a large proportion of soluble sulphur in a mafic magma would be distributed in an exhalative saline fluid as sulphate (Newton and Manning 2005). Solubility thus increases substantially with salinity (Blounot and Dickson 1969; Newton and Manning 2005). In the late magmatic stages of crystallisation, sulphides can oxidise and release metals and sulphur into the exsolved fluids (Candela and Holland 1986; Candela 1992; Audétat et al. 2004). The magmatic oxidation may have allowed the incorporation of sulphur into the saline (Cl brines) metasomatic fluids, which oxidised it to form sulphates trapped by the sapphires at high temperatures, forming anhydrite crystals. Evidence supporting the salinity of the metasomatic fluids is the presence of chlorine in some solid anhydrite inclusions (Fig. 12).

Regarding the origin of sulphur, it is proposed that much of the sulphur that allowed the formation of the anhydrite inclusions into sapphires comes from magmatic/hydrothermal fluids from the La Brea Pluton. This statement is because the Lower Cretaceous intrusives belonging to the Chilean coastal batholithic in the Atacama Region are associated with the formation of mineral deposits (e.g. IOCG

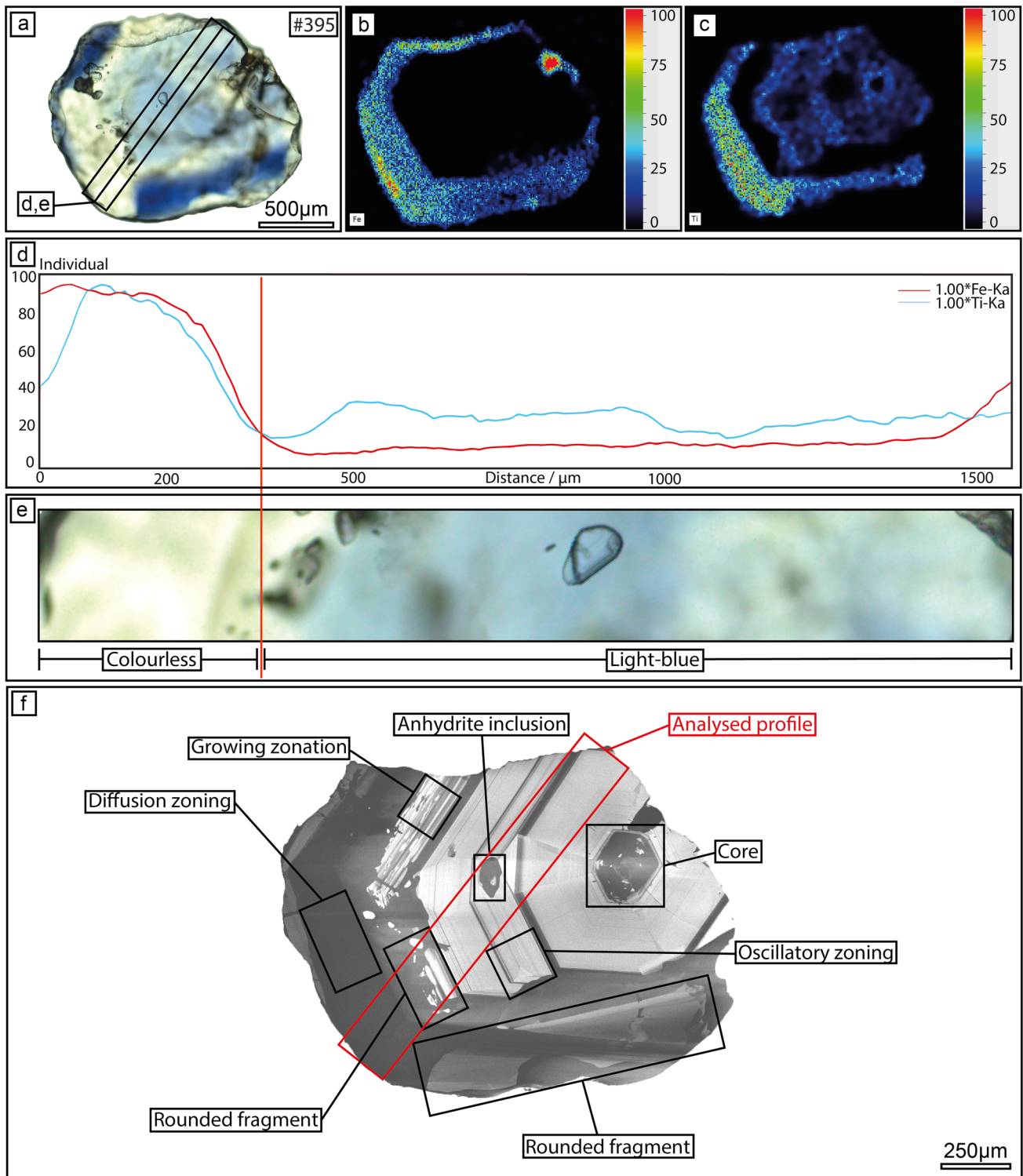


Fig. 11 Micro-XRF elemental distribution maps, SEM-CL micro-textures and colour relationship of the *sapphire* #395. **(a)** Multi-focus transmitted-light photograph indicating the location of the analysed μ -XRF line scan. **(b–c)** Elemental distribution maps of Fe and Ti trace the inner and outer rims in **(b)** and **(c)**, respectively. **(d)** The elemental line scan shows that the high Fe- and Ti-intensity peaks are

related to colourless zones, whereas the light-blue colour corresponds to low intensities. **(e)** Multi-focus transmitted-light photograph of the line scan location, showing the colour differences. **(f)** SEM-CL image of the *sapphire* #395 with all identified micro-textures, such as the irregular core, growing zonation, oscillatory zoning, micro-brecciation, and diffusion zoning

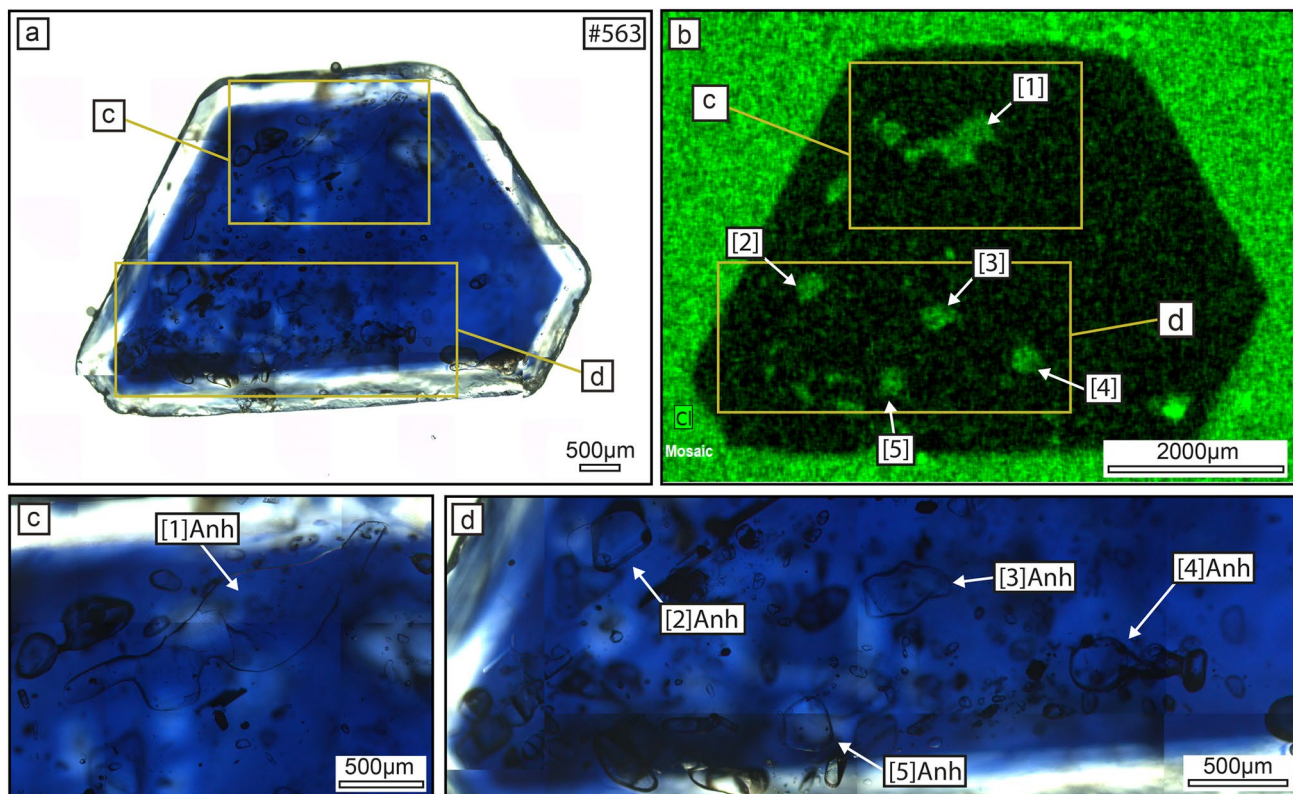


Fig. 12 Optical microscope microphotograph, and Micro-XRF elemental distribution map of *Sapphire #563*. (a) Microphotograph displays the blue inner zone with an external colourless rim, wherein the inclusions stand out. (b) Cl elemental distribution map of (a), where

zones with Cl concentrations correlate with anhydrite inclusions. (c–d) Microphotograph of anhydrite inclusions of (a), which are correlated with (b)

deposits), which are characterised by being largely oxidised and enriched in sulphur (Creixell et al. 2020; Marschik et al. 2000; Richards 2011). Notwithstanding this precedent, the contribution of sulphur from the basaltic units of the La Negra Formation cannot be discarded.

The rutile inclusions in sapphires can provide information about the formation conditions and the rutile solubility, which can be discussed regarding the Ti concentration (Peretti et al. 1996). Experiments confirm that rutile is highly soluble in fluids composed of H₂O and hydroxy-fluoride (HF) due to the formation of Ti-hydroxy-fluoride complexes (Ried 1994; Peretti et al. 1996), as it is also known that rutile solubility depends on P, T, and HF-concentration (Passaret et al. 1972; Ayers and Watson 1991; Ried 1994; Peretti et al. 1996). Higher fluoride concentration in the solution and lower pH thus favour rutile dissolution (Ayers and Watson 1991). Experimental studies at temperatures between 500 and 550 °C and pressures of 2–2.5 kbar have determined that the solubility of rutile in HF-H₂O fluids increases dramatically with increasing temperature and HF-concentration, whereas the changes are minor when varying the pressure (Ried 1994; Peretti et al. 1996). In the case of high-grade metamorphic fluids, TiO₂ is highly soluble due

to the presence of Cl-rich brines, or even more so in F-rich brines, which makes it highly dependent on the chemical environment and temperature (Rapp et al. 2010). Cl-brines' presence during the PPB sapphire formation may have allowed the mobility of Ti at high temperatures, incorporating it as a trace element in the sapphires. As the temperature decreases, the Ti becomes immobilised and precipitated as

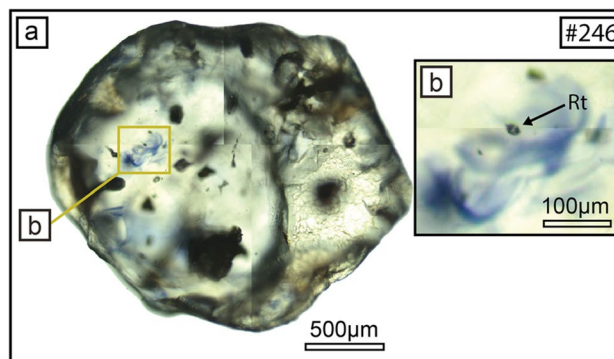


Fig. 13 Multi-focus transmitted-light photograph of *Sapphire #246*. (a) Colourless sapphire with rutile inclusions. (b) Selected zone from (a), irregular blue zones surround the rutile inclusions

rutile, trapped by the sapphires during growth. Some colourless sapphires present irregular blue areas near rutile inclusions, which could be related to Ti release from inclusions due to temperature increase (Fig. 13). A similar phenomenon occurs when heat treatments enhance the colour of sapphires and other gemstones. When high-temperature heat treatment is applied on sapphires, the rutile and spinel inclusions are dissolved, and the elements are released (Fritsch and Rossman 1988), increasing clarity and inducing blue colouration (Nassau 1981; Emmett and Douthit 1993; Shor and Weldon 2009). In the case of PPB, the coloured areas indicate metasomatism temperature and condition fluctuations, wherein the previously formed rutile inclusions are dissolved, releasing Ti, which is then incorporated into the sapphire structure through diffusion. The released Ti from inclusions, in combination with Fe in sapphires, can form pairs of $\text{Fe}^{2+}\text{-O-Ti}^{4+}$, allowing IVCT to yield the interaction through $\text{Fe}^{2+}\text{---}\text{Ti}^{4+}$ forming blue colouration (Fritsch and Rossman 1988; Themelis 1992; Bgasheva et al. 2012; Giuliani et al. 2014), so the Ti presence is essential, as the blue colour cannot develop without it (Nassau 1981).

Tube-like voids in some PPB sapphires can be interpreted as crystal growth dislocations. These voids have also been identified in rubies and they can be formed due to dissolution if the supersaturation decreases after the crystal growth or by trapped syngenetic solid inclusions producing dislocations (Pignatelli et al. 2020), which are due to overgrowth and entrapment of solid syngenetic inclusions, promoting "lattice closure errors" that become the origin of these dislocations (Klapper 2000, 2010; Pignatelli et al. 2020). The dislocations' direction is directly related to the shape, the orientation of growth faces and the growth front. It should also be noted that inclusions larger than 50 μm generally produce many dislocations. Regarding genetic significance, dislocations are essential because they allow crystal formation at low supersaturation fluid and supercooling (Klapper 2000, 2010).

Correlation between colour distributions and micro-textures

Even though sapphires have been analysed in their basal sections, it has been determined that colour distribution directly relates to micro-textures and, thus, formation stages. The type I sapphires were formed during regular periods when conditions did not vary. For example, blue, light-blue, dark-blue, and, to a lesser extent, colourless sapphires were formed during the first stage of regular growth, whereas the colourless zones generally formed during the fifth stage of diffusion zoning. Concerning type II and type III sapphires, the coloured zones are related to the z-axis, so it assumes they developed during the first regular growth and subsequent diffusion zoning stages. In type IV and type V

sapphires, the coloured areas are irregular and can, therefore, be considered irregular fragments due to the micro-brecciation processes, whereas the colourless zones can be mainly related to the late stage of diffusion zoning. The type VI sapphires are related to the second progressive and oscillatory zoning stage. Finally, type VII sapphires are associated with all formation stages.

Summary and conclusions

The PPB's multi-coloured sapphires are characterised by euhedral crystals ranging in size from hundreds of microns to about 3 mm, formed during a multi-stage heterogeneous metasomatic environment with an open system behaviour, wherein nucleation predominates over mineral growth.

Five stages have been defined, which can be identified in most sapphires and are described below (Fig. 14):

The first stage consists of the development of cores, which are generally homogeneous, indicating an initial growth rate where element concentration remain constant and do not fluctuate; a growth by zoning characterises the second stage, which allows the formation of the progressive and oscillatory zoning, demonstrating a chemical imbalance in the fluid-crystal interface; the third stage starts after decreasing the temperature allowing fragile tectonic deformation, producing micro-brecciation in the already-formed sapphires and subsequent dissolution due to temperature fluctuations, where the fragments, in some cases, show rounded edges, which may be due to variations in the forming conditions that make the sapphires unstable, allowing their dissolution; the fourth stage starts with the re-arrangement of sapphire fragments and subsequent overgrowth of new sapphires which incorporate them; The fifth stage is related to the formation of irregular colourless Fe-Ti outer rings in reconstituted sapphires.

Concerning colours and trace elements, the main trace elements detected are Fe, Ti, and Cr, to a lesser extent, varying across the primary growth textures and producing differences in colours and CL signal. It has also been determined that the colours are formed due to Fe and Ti trace elements, which should generally interact through the IVCT, whereas in some cases, these trace elements produce absorption in the non-visible light spectrum and thus form colourless sapphires. The first stages of sapphire formation are generally related to blue shades, whereas colourless is more common in late stages linked to diffusion zoning. Regarding the CL Signal, Cr^{3+} and Ti^{3+} play an essential role in visualising micro-textures due to their luminescence. The Cr^{3+} is associated with cores and early formation stages unless sapphires have been dissolved and reprecipitated.

The solid inclusions identified are andalusite, rutile and anhydrite. In addition, Fe-Ti bearing inclusions have

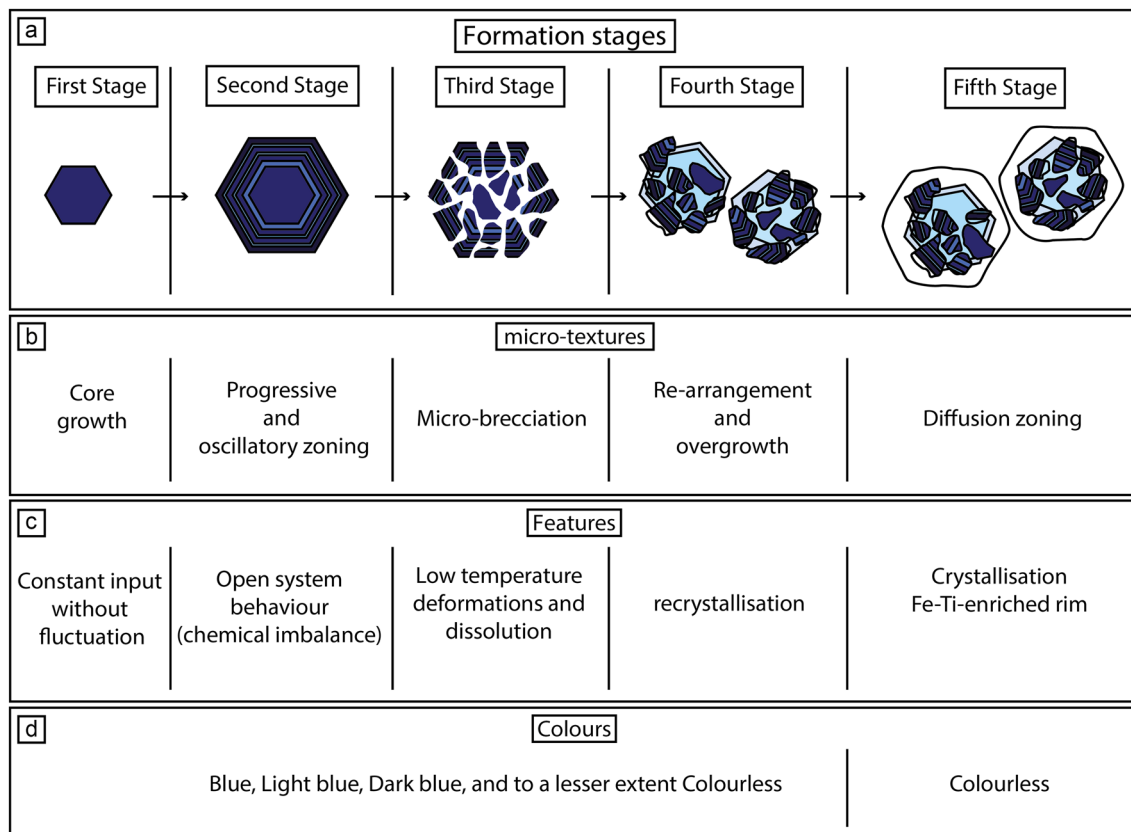


Fig. 14 Formation stages of the PPB sapphires, in which 5 stages have been defined according to the sapphires' micro-textures. **(a)** Representative scheme of formation stages. **(b)** Main micro-textures

of each formation stage. **(c)** Main features of the respective formation stages. **(d)** Colours related to each formation stage

been identified by micro-XRF, suggesting the presence of ilmenite, but this has not yet been confirmed due to the absence of Raman data. It was proposed that the andalusite formed before being trapped by sapphire crystallisation because they are euhedral prismatic crystals indicating contact metasomatism of varying temperatures and low pressures. Anhydrite inclusions are associated with large anhedral crystals, considered primary and formed during crystal growth, and smaller secondary anhedral inclusions, found in clusters due to secondary alteration features. The anhydrite inclusions indicate oxidised magmatic/metasomatic fluids, confirming the presence of S in the system, which may have been incorporated from the host rock or magmatic fluids. Additionally, the presence of Cl in anhydrite inclusions confirms the presence of CL-bearing brines, which increase the rutile solubility at high temperatures. The rutile inclusions are mostly located in sapphires' outer rims and were formed during the temperature drop that causes a decrease in Ti solubility. It should be noted that some solid rutile inclusions have been dissolved by the subsequent temperature increase, releasing the Ti into the sapphires and thus producing colour.

In conclusion, the PPB's sapphires were formed due to a five-stage heterogeneous metasomatism, in which low pressures predominated whilst the temperature rose and fell. This metasomatism is characterised by being highly oxidised and enriched in sulphur, which forms the anhydrite inclusions. In addition, andalusite and rutile inclusions are present. The crystals have traces of Fe–Ti–Cr, which varied as the sapphires developed, expressed in the colour variations.

Supplementary Information The online version contains supplementary material available at <https://doi.org/10.1007/s00531-024-02391-0>.

Acknowledgements This research was made possible by several sources of funding and support. A scholarship (Award number: 91683910) from the German Academic Exchange Service (DAAD) provided financial support for the research. The Fission Track Lab at TU-BAF assisted with sample preparations, whilst the Biology Institute at TU-BAF, with the Krüger Foundation's sponsorship, provided the microscope that made the multi-focus transmitted-light photographs. The Centre for Efficient High-Temperature Material Conversion (ZeHS) and the Geology Institute at TU-BAF supported the Raman analyses, and the Mineralogy Institute and the Geology Institute at TU-BAF supported the OM-CL and SEM-CL analyses, respectively. Bruker Nano Berlin GmbH provided the analysis and support for the Micro-XRF analyses. The contributions of Dr Bastian Wauschkuhn,

Jun. Prof. Dr Ing. Sindy Fuhrmann, and Prof. Dr Jens Götze were also integral to the successful completion of this research project.

Authors contribution All authors contributed to the study conception and design. Material preparation, data collection and analysis were performed by Gustavo Miranda-Díaz, Andrew Menzies, Karl Riveros-Jensen, Gerhard Heide, Lena Bußmann, Birk Härtel, Roald Tagle, Eduardo Medina, Wolfgang Griem. The first draft of the manuscript was written by Gustavo Miranda-Díaz, and all authors commented on previous versions of the manuscript. All authors read and approved the final manuscript.

Funding Open Access funding enabled and organized by Projekt DEAL. A scholarship (Award number: 91683910) from the German Academic Exchange Service (DAAD) assigned to Dipl. -Geol. Gustavo Miranda-Díaz provided financial support for the research.

Data availability The authors confirm that the data supporting the findings of this study are available within the article [and/or] its supplementary materials.

Declarations

Conflicts of interest All authors certify that they have no affiliations with or involvement in any organisation or entity with any financial interest or non-financial interest in the subject matter or materials discussed in this manuscript.

Open Access This article is licensed under a Creative Commons Attribution 4.0 International License, which permits use, sharing, adaptation, distribution and reproduction in any medium or format, as long as you give appropriate credit to the original author(s) and the source, provide a link to the Creative Commons licence, and indicate if changes were made. The images or other third party material in this article are included in the article's Creative Commons licence, unless indicated otherwise in a credit line to the material. If material is not included in the article's Creative Commons licence and your intended use is not permitted by statutory regulation or exceeds the permitted use, you will need to obtain permission directly from the copyright holder. To view a copy of this licence, visit <http://creativecommons.org/licenses/by/4.0/>.

References

- Allègre CJ, Provost A, Jaupart C (1981) Oscillatory zoning: A pathological case of crystal growth. *Nature* 294(5838):223–228. <https://doi.org/10.1038/294223a0>
- Althaus E (1967) The triple point andalusite – sillimanite – kyanite. *Contrib Miner Petrol* 16(1):29–44. <https://doi.org/10.1007/bf00371606>
- Arabasz WJ Jr (1971) Geological and geophysical studies of the Atacama fault zone in northern Chile (Doctoral dissertation). California Institute of Technology. <https://doi.org/10.7907/IQCV-NG11>
- Arévalo C (2005) Carta Copiapó, Región de Atacama. Servicio Nacional de Geología y Minería. Carta geológica de Chile, serie geología básica: 91, 54.
- Audétat A, Pettko T, Dolejš D (2004) Magmatic anhydrite and calcite in the ore-forming quartz-monzodiorite magma at Santa Rita, New Mexico (USA): genetic constraints on porphyry-Cu mineralization. *Lithos* 72(3–4):147–161. <https://doi.org/10.1016/j.lithos.2003.10.003>
- Ayers JC, Watson EB (1991) Solubility of apatite, monazite, zircon, and rutile in supercritical aqueous fluids with implications for subduction zone geochemistry. *Philos Transact A Math Phys Eng Sci* 335(1638):365–375. <https://doi.org/10.1098/rsta.1991.0052>
- Baker LL, Rutherford MJ (1996) Crystallisation of anhydrite-bearing magmas. In M. P. Brown & J. F. H. Thompson (Eds.), *The Third Hutton Symposium on the Origin of Granites and Related Rocks*, Geological Society of London, pp 243–258. <https://doi.org/10.1130/0-8137-2315-9.243>
- Bard JP (1986) *Microtextures of igneous and metamorphic rocks* (Vol. 1) Springer Science & Business Media.
- Barker AJ (1998) *Introduction to Metamorphic Textures and Microstructures* (1st ed.). Routledge. <https://doi.org/10.4324/9781315831626>
- Barth AP, Dorais MJ (2000) Magmatic anhydrite in granitic rocks: First occurrence and potential petrologic consequences. *Am Miner* 85(3–4):430–435. <https://doi.org/10.2138/am-2000-0404>
- Berg K, Tidy E (2009) Descubrimiento de zafiros en Chile. In *Proceedings of the XII Congreso Geológico Chileno*, pp 20–23.
- Bernard A, Demaiffe D, Mattielli N, Punongbayan RS (1991) Anhydrite-bearing pumices from Mount Pinatubo: Further evidence for the existence of sulphur-rich silicic magmas. *Nature* 354(6349):139–140. <https://doi.org/10.1038/354139a0>
- Bgasheva TV, Ahmetshin EA, Zharikov EV (2012) Heat treatment enhancement of natural orange-red sapphires. *Adv Mater Sci*. <https://doi.org/10.2478/v10077-012-0006-3>
- Blasse G, Verweij JWM (1990) The luminescence of titanium in sapphire laser material. *Mater Chem Phys* 26(2):131–137. [https://doi.org/10.1016/0254-0584\(90\)90033-7](https://doi.org/10.1016/0254-0584(90)90033-7)
- Blount CW, Dickson FW (1969) The solubility of anhydrite (CaSO₄) in NaCl-H₂O from 100 to 450 C and 1 to 1000 bars. *Geochim Cosmochim Acta* 33(2):227–245. [https://doi.org/10.1016/0016-7037\(69\)90140-9](https://doi.org/10.1016/0016-7037(69)90140-9)
- Bradt RC (2008) The sillimanite minerals: andalusite, kyanite, and sillimanite. In J. F. Shackelford & R. H. Doremus (Eds.), *Ceramic and Glass Materials*. pp. 41–48. <https://doi.org/10.1007/978-0-387-73362-3>
- Brown M, Diaz F, Grocott J (1993) Displacement history of the Atacama fault system 25°00'S–27°00'S, northern Chile. *Geol Soc Am Bull* 105(9):1165–1174. [https://doi.org/10.1130/0016-7606\(1993\)105%3c1165:DHOTAF%3e2.3.CO;2](https://doi.org/10.1130/0016-7606(1993)105%3c1165:DHOTAF%3e2.3.CO;2)
- Candela PA (1992) Controls on ore metal ratios in granite-related ore systems: an experimental and computational approach. *Earth Environ Sci Trans R Soc Edinb* 83(1–2):317–326. <https://doi.org/10.1017/s0263593300007999>
- Candela PA, Holland HD (1986) A mass transfer model for copper and molybdenum in magmatic hydrothermal systems; the origin of porphyry-type ore deposits. *Econ Geol* 81(1):1–19. <https://doi.org/10.2113/gsecongeo.81.1.1>
- Carroll MR, Rutherford MJ (1987) The stability of igneous anhydrite: experimental results and implications for sulfur behavior in the 1982 El Chichon trachyandesite and other evolved magmas. *J Petrol* 28(5):781–801. <https://doi.org/10.1093/ptrology/28.5.781>
- Chambefort I, Dilles JH, Kent AJ (2008) Anhydrite-bearing andesite and dacite as a source for sulfur in magmatic-hydrothermal mineral deposits. *Geology* 36(9):719–722. <https://doi.org/10.1130/G24920A.1>
- Chapoulièr R, Capdupuy C, Schwoerer M, Bechtel F (1999) Cathodoluminescence and crystal growth of sapphire. *Phys Stat Sol (a)* 171(2):613–621
- Clarke DB, Dorais M, Barbarin B, Barker D, Cesare B, Clarke G, El Baghdadi M, Erdmann S, Förster HJ, Gaeta M, Gottesmann B et al (2005) Occurrence and origin of andalusite in peraluminous felsic igneous rocks. *J Petrol* 46(3):441–472. <https://doi.org/10.1093/ptrology/egh083>
- Creixell C, Fuentes J, Bierma H, Salazar E (2020) Tectonic setting of Cretaceous porphyry copper deposits of northern Chile (28°–30°

- S) and its relations with magmatic evolution and metallogeny. *Andean Geology* 47(3):469–507. <https://doi.org/10.5027/andgeoV47n3-3035>
- Emmett JL, Douthit TR (1993) Heat treating the sapphires of Rock Creek Montana. *Gems & Gemology* 29(4):250–272. <https://doi.org/10.5741/gems.29.4.250>
- Ferguson J, Fielding PE (1971) The origins of the colours of yellow, green and blue sapphires. *Chem Phys Lett* 10(3):262–265. [https://doi.org/10.1016/0009-2614\(71\)80282-8](https://doi.org/10.1016/0009-2614(71)80282-8)
- Ferguson J, Fielding PE (1972) The origins of the colours of natural yellow, blue, and green sapphires. *Aust J Chem* 25(7):1371–1385. <https://doi.org/10.1071/CH9721371>
- Fritsch E, Rossman GR (1987) An update on color in gems. Part 1: Introduction and colors caused by dispersed metal ions. *Gems & Gemology* 23 3 126 139. <https://doi.org/10.5741/GEMS.23.3.126>
- Fritsch E, Rossman GR (1988) An update on color in gems. Part 2: Colors involving multiple atoms and color centers. *Gems & Gemology* 24 1, 3 15. <https://doi.org/10.5741/GEMS.24.1.3>
- Gaft M, Reisfeld R, Panczer G (2015) *Modern luminescence spectroscopy of minerals and materials*. Springer. <https://doi.org/10.1007/978-3-319-24765-6>
- Giuliani G, Groat LA (2019) Geology of corundum and emerald gem deposits. *Gems & Gemology* 55(4). <https://doi.org/10.5741/GEMS.55.4.464>
- Giuliani G, Ohnenstetter D, Fallick AE, Groat L, Fagan A (2014) The geology and genesis of gem corundum deposits. In L. A. Groat (Ed.), *Geology of gem deposits*. Mineralogical Association of Canada, pp. 29–112. ISBN 9780921294542
- Götze J, Schertl HP, Neuser RD, Kempe U, Hanchar JM (2013) Optical microscope-cathodoluminescence (OM–CL) imaging as a powerful tool to reveal internal textures of minerals. *Mineral Petrol* 107(3):373–392. <https://doi.org/10.1007/s00710-012-0256-0>
- Grocott J, Brown M, Dallmeyer RD, Taylor GK, Treloar PJ (1994) Mechanisms of continental growth in extensional arcs: An example from the Andean plate-boundary zone. *Geology* 22(5):391–394. [https://doi.org/10.1130/0091-7613\(1994\)022%3C0391:MOCGIE%3E2.3.CO;2](https://doi.org/10.1130/0091-7613(1994)022%3C0391:MOCGIE%3E2.3.CO;2)
- Gugushev C, Götze J, Göbbels M (2010) Cathodoluminescence microscopy and spectroscopy of synthetic ruby crystals grown by the optical floating zone technique. *Am Miner* 95(4):449–455. <https://doi.org/10.2138/am.2010.3291>
- Holdaway MJ, Mukhopadhyay B (1993) A reevaluation of the stability relations of andalusite: Thermochemical data and phase diagram for the aluminum silicates. *Am Miner* 78(3–4):298–315
- Hughes RW, Monorotkul W, Hughes EB (2017) *Ruby & sapphire: A gemologist's guide*. RWH Publishing/Lotus Gemology.
- Hughes RW (1997) *Ruby and sapphire*. RWH publishing.
- Jugo PJ, Luth RW, Richards JP (2005) An experimental study of the sulfur content in basaltic melts saturated with immiscible sulfide or sulfate liquids at 1300°C and 1.0 GPa. *J Petrol* 46(4):783–798. <https://doi.org/10.1093/petrology/egh097>
- Kane RE, Kammerling RC, Koivula JI, Shigley JE, Fritsch E (1990) The identification of blue diffusion-treated sapphires. *Gems & Gemology* 26(2):115–133. <https://doi.org/10.5741/gems.26.2.115>
- Kempe U, Götze J (2002) Cathodoluminescence (CL) behaviour and crystal chemistry of apatite from rare-metal deposits. *Mineral Mag* 66(1):151–172. <https://doi.org/10.1180/0026461026610019>
- Klapper H (2000) Generation and propagation of dislocations during crystal growth. *Mater Chem Phys* 66(2–3):101–109. [https://doi.org/10.1016/S0254-0584\(00\)00342-4](https://doi.org/10.1016/S0254-0584(00)00342-4)
- Klapper H (2010) Generation and Propagation of Defects During Crystal Growth. In G. Dhanaraj, K. Byrappa, V. Prasad, & M. Dudley (Eds.), *Springer Handbook of Crystal Growth*. Springer, pp 55–87. https://doi.org/10.1007/978-3-540-74761-1_4
- Liu E (2015) Flower-shaped Trapiche Ruby from Mong Hsu, Myanmar. *J Gemmol* 34(8): 660–662.
- Luhr JF, Carmichael IS, Varekamp JC (1984) The 1982 eruptions of El Chichón Volcano, Chiapas, Mexico: mineralogy and petrology of the anhydrite bearing pumices. *J Volcanol Geoth Res* 23(1–2):69–108. [https://doi.org/10.1016/0377-0273\(84\)90057-X](https://doi.org/10.1016/0377-0273(84)90057-X)
- Marfunin AS (1979) *Spectroscopy, Luminescence and Radiation Centers in Minerals*. Springer Verlag. <https://doi.org/10.1007/978-3-642-67112-8>
- Marschik R, Leveille RA, Martin W, Porter TM(2000) La Candelaria and the Punta del Cobre district, Chile: Early Cretaceous iron oxide cu-au (-Zn-Ag) mineralization. In: Porter TM (Ed.). *Hydrothermal iron oxide copper-gold and related deposits: a global perspective*. PGC Publishing: Adelaide. 1 pp. 163 175
- Miranda-Díaz G, Riveros-Jensen K, Heide G, Menzies A, Griem W, Araya-Tabilo E, Añasco-Leyton G, Medina E (2022) Geology and mineralogy of sapphire-rich metasomites (sapphirites) deposit at the Portezuelo de Pajas Blancas, northern Chile: Genetic implications for unusual metasomatic processes in the Central Andes. *Ore Geol Rev* 141:104646. <https://doi.org/10.1016/j.oregeorev.2021.104646>
- Miranda-Díaz G (2024) *Origin of sapphire deposits, Portezuelo de Pajas Blancas area: mineralogical, geochemical, and crystallographic aspects, Atacama Region – Chile* [In preparation doctoral dissertation], Technische Universität Bergakademie Freiberg.
- Nasdala L, Götze J, Hanchar JM, Gaft M, Krbetschek MR (2004) Luminescence techniques in earth sciences. In: Beran A, Libowitzky E (Eds) *Spectroscopic methods in mineralogy*. European Mineralogical Union Notes in Mineralogy, 6, pp 43–91. <https://doi.org/10.1180/EMU-notes.6.2>
- Nassau K (1981) Heat treating ruby and sapphire: technical aspects. *Gems & Gemology* 17(3):121–131. <https://doi.org/10.5741/gems.17.3.121>
- Neuser RD, Bruhn F, Götze J, Habermann D, Richter DK (1995) *Kathodolumineszenz: Methodik und anwendung*. Zentralblatt Für Geologie Und Paläontologie, Teil I, H 1(2):287–306
- Newton RC (1966) Kyanite-Andalusite Equilibrium from 700° to 800°C. *Science* 153(3732):170–172. <https://doi.org/10.1126/science.153.3732.170>
- Newton RC, Manning CE (2005) Solubility of anhydrite, CaSO₄, in NaCl–H₂O solutions at high pressures and temperatures: applications to fluid–rock interaction. *J Petrol* 46(4):701–716. <https://doi.org/10.1093/petrology/egh094>
- Nikolskaya LV, Terekhova VM, Samoilovich MI (1978) On the origin of natural sapphire color. *Phys Chem Miner* 3(3):213–224. <https://doi.org/10.1007/BF00633571>
- Ortoleva P, Merino MC, Chadam J (1987) Geochemical self-organization I; reaction-transport feedbacks and modeling approach. *Am J Sci* 287(10):979–1007. <https://doi.org/10.2475/ajs.287.10.979>
- Pagel M, Barbin V, Blanc P, Ohnenstetter D (2000) Cathodoluminescence in Geoscience: An Introduction. In: Pagel M, Barbin V, Blanc P, Ohnenstetter D (Eds) *Cathodoluminescence in Geoscience*, Springer-Verlag Berlin Heidelberg, pp 1–16. https://doi.org/10.1007/978-3-662-04086-7_1
- Palke AC (2020) Coexisting rubies and blue sapphires from major world deposits: a brief review of their mineralogical properties. *Minerals* 10(5):472. <https://doi.org/10.3390/min10050472>
- Parat F, Dungan MA, Streck MJ (2002) Anhydrite, pyrrhotite, and sulfur-rich apatite: tracing the sulfur evolution of an Oligocene andesite (Eagle Mountain, CO, USA). *Lithos* 64(3–4):63–75. [https://doi.org/10.1016/S0024-4937\(02\)00155-X](https://doi.org/10.1016/S0024-4937(02)00155-X)
- Passaret M, Toudic Y, Regreny A, Aumont R, Bayon JF (1972) Recrystallisation de TiO₂, GeO₂, Si1–xGexO₂ en solutions hydrothermales fluorées. *J Cryst Growth* 13:524–529. [https://doi.org/10.1016/0022-0248\(72\)90292-8](https://doi.org/10.1016/0022-0248(72)90292-8)
- Peretti A, Mullis J, Mouawad F (1996) The role of fluorine in the formation of colour zoning in rubies from Mong Hsu, Myanmar

- (Burma). *The Journal of Gemmology*, 25(1), pp 3–19. <https://doi.org/10.15506/JoG.1996.25.1.3>
- Pignatelli I, Morlot C, Cathelineau M, Giuliani G, Liu S (2020) Ruby from Mong Hsu, Myanmar: a revised growth mechanism. *The Journal of Gemmology* 37(4):404–415
- Ponahlo J (2000) Cathodoluminescence as a tool in gemstone identification. In: Pagel M, Barbin V, Blanc P, Ohnenstetter D (Eds) *Cathodoluminescence in Geoscience*, Springer-Verlag Berlin Heidelberg, pp 479–500. <https://doi.org/10.1007/978-3-662-04086-7>
- Rakotondrazafy AFM, Giuliani G, Ohnenstetter D, Fallick AE, Rakotosamizanany S, Andriamamonjy A, Ralantoarison T, Razanetseho M, Offant Y, Garnier V, Maluski H, Dunaigre C, Schwarz D, Ratriho V (2008) Gem corundum deposits of Madagascar: A review. *Ore Geol Rev* 34(1–2):134–154. <https://doi.org/10.1016/j.oregeorev.2007.05.001>
- Rapp JF, Klemme S, Butler IB, Harley SL (2010) Extremely high solubility of rutile in chloride and fluoride-bearing metamorphic fluids: An experimental investigation. *Geology* 38(4):323–326. <https://doi.org/10.1130/G30753.1>
- Remond G, Phillips MR, Roques-Carnes C (2000) Importance of instrumental and experimental factors on the interpretation of cathodoluminescence data from wide band gap materials. In: Pagel M, Barbin V, Blanc P, Ohnenstetter D (Eds) *Cathodoluminescence in Geoscience*, Springer-Verlag Berlin Heidelberg, pp 59–126. https://doi.org/10.1007/978-3-662-04086-7_4
- Richards JP (2011) High Sr/Y arc magmas and porphyry Cu±Mo±Au deposits: Just add water. *Econ Geol* 106(7):1075–1081. <https://doi.org/10.2113/econgeo.106.7.1075>
- Ried FA (1994) Titanmobilität i.e. Titanmobilität: Metasomatische, titanreiche Adern am Kontakt von Dolomitmarmoren zur Bergeller Intrusion. Dissertation, ETH Zurich. <https://doi.org/10.3929/ethz-a-001382248>
- Roedder E, Patterson DA (1982) Fluid inclusions in gemstones: Valuable defects. In *International Gemological Symposium Proceedings*. Gemological Institute of America, pp 479–502.
- Schmetzer K, Kiefert L (1990) Spectroscopic evidence for heat treatment of blue sapphires from Sri Lanka — additional data. *The Journal of Gemmology*, 22(2), pp 80–82. <https://doi.org/10.15506/jog.1990.22.2.80>
- Schmetzer K, Beili Z, Yan G, Bernhardt HJ, Hänni HA (1999) Element mapping of trapiche rubies. *The Journal of Gemmology*, 26(5), pp 289–301. <https://doi.org/10.15506/JoG.1999.26.5.289>
- Sherman J (1955) The theoretical derivation of fluorescent X-ray intensities from mixtures. *Spectrochim Acta* 7(5):283–306. [https://doi.org/10.1016/0371-1951\(55\)80041-0](https://doi.org/10.1016/0371-1951(55)80041-0)
- Shor R, Weldon R (2009) Ruby and sapphire production and distribution: A quarter century of change. *Gems & Gemology* 45(4):236–259. <https://doi.org/10.5741/gems.45.4.236>
- Streck MJ, Dilles JH (1998) Sulfur evolution of oxidized arc magmas as recorded in apatite from a porphyry copper batholith. *Geology* 26(6):523–526. [https://doi.org/10.1130/0091-7613\(1998\)026%3c0523:SEOOAM%3e2.3.CO;2](https://doi.org/10.1130/0091-7613(1998)026%3c0523:SEOOAM%3e2.3.CO;2)
- Themelis T (1992) *The Heat Treatment of Ruby and Sapphire*. Gemlab Inc., U.S.A.
- Townsend MG (1968) Visible charge transfer band in blue sapphire. *Solid State Commun* 6(2):81–83. [https://doi.org/10.1016/0038-1098\(68\)90005-7](https://doi.org/10.1016/0038-1098(68)90005-7)
- Tracy RJ (1982) Compositional zoning and inclusions in metamorphic minerals. In: Ferry JM (Eds) *Characterisation of metamorphism through mineral equilibria*, *Reviews in Mineralogy & Geochemistry*, 10, pp 354–398. <https://doi.org/10.1515/9781501508172-013>
- Walker G (1985) Mineralogical Applications of Luminescence Techniques. In: Berry FJ, Vaughan DJ (Eds) *Chemical Bonding and Spectroscopy in Mineral Chemistry*, pp 103–140. https://doi.org/10.1007/978-94-009-4838-9_4
- Weill DF, Fyfe WS (1961) A preliminary note on the relative stability of andalusite, kyanite, and sillimanite. *Am Miner* 46:1275–1280
- Yardley BWD, Rochelle CA, Barnicoat AC, Lloyd GE (1991) Oscillatory zoning in metamorphic minerals: An indicator of infiltration metasomatism. *Mineral Mag* 55(380):357–365. <https://doi.org/10.1180/minmag.1991.055.380.06>
- Yu H, Clarke DR (2002) Effect of codoping on the R-Line luminescence of Cr³⁺-doped Alumina. *J Am Ceram Soc* 85(8):1966–1970. <https://doi.org/10.1111/j.1151-2916.2002.tb00389.x>